Synthesis Process of Au-Fe/Al_2O_3 Catalysts for Methane Combustion

Mery Sheryll Hernández Maya

Thesis Dissertation to Qualify for Master's Degree in Chemical Engineer

Director

Víctor Gabriel Baldovino Medrano

Co-Directors

Edwing Alexander Velasco Rozo

Luz Marina Ballesteros Rueda

Universidad Industrial De Santander

Department Of Chemical Engineer

Faculty Of Physicochemicals

Bucaramanga

2021

To all my family.

"What we know is a drop, what we don't know is an ocean" I.N.

Acknowledgment

This work was financed by *Agencia Nacional de Hidrocarburos (ANH)* and *Minciencias*, Colombia, within the frame of the project 1102-721-50962: *"Desarrollo de alternativas catalíticas para la reducción y valorización de emisiones de gases de efecto invernadero típicas de pozos y refinerías petroleras por combustión catalítica de VOCs y transformación de CO_2 y CH_4 en gas de síntesis"*

Content

Tables

Figures

Appendices

Abstract

Title: Synthesis process of Au-Fe/Al_2O_3 catalysts for methane combustion*

Authors: Mery S. Hernández-Maya**

Keywords: Methane combustion, Au-Fe/Al_2O_3, sequential impregnation, light off.

Description: Catalytic methane combustion is a reaction of interest to reduce greenhouse gas emissions from gas flaring processes. Some considerations must be done when synthesizing catalysts for this specific reaction. In this work, a series of Au-Fe/Al_2O_3 catalysts were synthesized through a sequential impregnation process designed considering the chemical processes occurring at each step. Catalysts were synthesized with a total molar concentration of metals of 10 μmol/m^2 (support) and with Au/(Au+Fe) molar ratios of 0.0, 0.02, 0.09, 0.29 and 1.00. These catalysts behaved in methane combustion (57.000 mL/(g*h) under lean conditions of 1.5 vol.% CH_4, 21 vol.% O_2, N_2 balanced) as follow: (1) Activity was observed since 500°C for all the catalysts (2) Only CO_2 and CO were detected on the product current with a 90% Selectivity to CO_2 (3) The catalyst with lower molar ratios showed the higher activity (4) In general, an inversed hysteresis was observed on the catalytic behavior. Such behavior implied the following: (A) The catalytic activity was found to be strongly dependent on the gold content, decreasing on increasing the gold composition (B) The differences observed in activity during temperature ignition and extinction was due to size increasing of gold nanoparticles (C) High gold dispersion and a possible synergistic behavior between Au and Fe was observed for the catalyst with the smaller molar ratio of 0.01 which presented an ignition temperature of ca. 523°C and 70% of methane conversion.

---

* Trabajo de grado

** Faculty of Physicochemical Engineers. Chemical Engineering Department. Director: Prof. Víctor Gabriel Baldovino Medrano. Co-directors: Prof. Luz Marina Ballesteros Rueda & Msc. Edwing Alexander Velasco Rozo.

Resumen

Título: Proceso de síntesis de catalizadores Au-Fe/Al_2O_3 para combustión de metano[†]

Autores: Mery S. Hernández-Maya[**]

Palabras clave: Combustión de metano, Au-Fe/Al_2O_3, impregnación secuencial, light off.

Descripción: La combustión catalítica de metano es una reacción de interés para reducir las emisiones de gases de efecto invernadero. Se deben tener en cuenta algunas consideraciones al sintetizar catalizadores para esta reacción específica. En este trabajo, se sintetizaron una serie de catalizadores Au-Fe/Al_2O_3 mediante un proceso de impregnación secuencial diseñado considerando los procesos químicos que ocurren en cada paso. Los catalizadores se sintetizaron con una concentración molar total de metales de 10 μmol/m^2 (soporte) y con relaciones molares Au/(Au+Fe) de 0.0, 0.02, 0.09, 0.29 y 1.00. Estos catalizadores se comportaron en la combustión de metano (57.000 mL/g* h, bajo condiciones diluidas de CH_4 de 1.5% vol en 21% vol. O_2, y N_2 balanceado) de la siguiente manera: (1) Se observó actividad desde 500 °C para todos los catalizadores (2) Solo se detectaron CO_2 y CO en la corriente de producto con una selectividad del 90% a CO_2 (3) El catalizador con relaciones molares más bajas mostró la actividad más alta (4) En general, se observó una histéresis inversa en el comportamiento catalítico. Tal comportamiento implicó lo siguiente: (A) Se encontró que la actividad catalítica era fuertemente dependiente del contenido de oro, disminuyendo al aumentar la composición de oro, (B) Las diferencias observadas en la actividad durante la ignición y extinción de la temperatura se debieron al aumento de tamaño de las nanopartículas de oro (C) Se observó una alta dispersión de oro y un posible comportamiento sinérgico entre Au y Fe para el catalizador con la relación molar menor de 0.01 que presentó una temperatura de ignición de ~523 °C y 70% de conversión de metano.

[†] Trabajo de grado

[**] Facultad de Ingenierías Fisicoquímicas. Escuela de Ingeniería Química. Director: Prof. Víctor Gabriel Baldovino Medrano. Codirectores: Prof. Luz Marina Ballesteros Rueda y Msc. Edwing Alexander Velasco Rozo.

Introduction

Gas flaring is a technique commonly used for the combustion of gaseous waste derived from different oil refining or extraction processes. Usually, such gaseous waste contain highly polluting volatile organic compounds (VOCs), and are rich in methane, which has a greenhouse effect potential almost 21 times greater than that of CO_2.[1] To eliminate unwanted gaseous waste, gas flaring is an attractive technique due to its low infrastructure costs based on burners or torches, as well as the simplicity to carry out the assembly even in areas of difficult access,[2,3] in addition to other technical aspects, such as the relative stability of the process, and operational aspects, due to the spontaneity of combustion. Despite these advantages, the use of torches has been highly questioned by various environmental and health organizations around the world, since in most cases the combustion is incomplete and takes place at very high temperatures (~1600 °C), which causes the indiscriminate emission of methane, CO_2, and by-products such as CO, volatile organic compounds, soot and NOx, among others.[4]

Catalytic combustion is an alternative to traditional flaring processes, since it allows complete combustion at temperatures up to three times lower than those of conventional burning, lowering NOx formation at concentrations below 5 ppm.[5,6] Even though it is a widely studied alternative, today it has not matured enough to be industrially implemented to replace, at least partially, the obsolete flaring technology. Today, the scientific and technological challenge of catalytic combustion focuses on the design and synthesis of very active, selective and stable catalysts,[7] but inexpensive, so that their scaling does not exceed the threshold of financial viability of the technology.

For catalytic combustion many heterogeneous catalysts have been studied based on noble metals, transition metal oxides and even bimetallic metal particles.[8,9] Noble metals, despite their high commercial price, are preferred because of their high specific activity.[10,11] Among noble metals, Au-based catalysts have attracted great attention for oxidation reactions such as CO oxidation, since they can exhibit high activity at lower temperatures when having a highly dispersed gold phase over the catalytic support.[12] In this sense, Haruta claimed that gold catalysts have an advantage over other noble metals in low temperature reactions of alkanes due to the lower bonding strength of adsorbates on Au defective sites compared to that on Pd and Pt,[13] Also, compare to a very active noble metal as palladium, gold is a more abundant and cheaper metal. However, for methane combustion Au-based catalysts have lost interest due to the costly and complicated synthesis control focused on particle size, which limit the catalytic activity. Recently, a new generation of catalysts based on a noble metal phase (highly dispersed and with small particle sizes) that works in cooperation with other low-cost metals has attracted again the interest in noble metal catalysts due to reducing the catalyst's synthesis cost while increasing its activity.[14] However, the latter have not been clearly documented for Au-based catalysts in methane combustion. Gold is unique in several aspects: it is the most electronegative metal, comparable to selenium, and only slightly more electropositive than sulfur and iodine.[15] Gold easily forms alloys with other metals, and intermetallic compounds of definite composition with copper, aluminum, tin, and titanium.[15] The reactivity of supported gold catalysts obeys two essential aspects: particle sizes and metal-support interaction.

About particle size, literature reports that Au particles dispersed on metal oxides must be smaller than 5 nm to obtain high catalytic activity in oxidation reactions of volatile organic

compounds.[11] High dispersion of the gold phase over the support is usually an important target to avoid sintering and large Au agglomerates that could result in inactive gold catalysts.[16] Also, small Au nanoparticles has been proved to be very efficient when integrated into bimetallic catalysts reporting higher catalytic activity due to Au promotion of the partner metal as in the case of Au-Sn or Au-Pt, among others.[17,18] In general, bimetallic catalysts based on noble metals tend to be better than supported monometallic catalysts regarding their high catalytic activity and selectivity for several reactions, which is often attributed to the synergy between metal nanoparticles.[19]

About the interaction between metal and support, the selection of a suitable support must be done carefully since it can affect the stability of the catalyst. For methane combustion, Au catalytic performance has been observed to depend not only on the particle size, but on the metal oxide chose as support.[20] In general, among transition metal oxides used as the support material, alumina is the most common support due to its availability of surface area and hydroxyl groups on the surface. Alumina supported gold catalysts have been studied in methane combustion using high gold loadings in the catalysts (ca. 5 wt%); but such loadings promote sintering followed by posterior deactivation.[21] Many other metallic oxides haven been studied as support for gold catalysts, from which iron oxide stands as the most promising since the activity is controlled by metal-support interactions.[22] The role of supports is to activate or to provide sites at the perimeter interface around gold particles for activating one of the reactants and supply it to the gold surface. The supports are required to have large specific surface areas, preferably larger than 50 m^2/g.[23] In the case of iron oxide, due to its oxidation-reduction capacity, it could be implemented as a promoter of active sites, providing stability, and reducing the cost of the active phase.[24] The disadvantage of the iron oxide as

support is the low surface area which provides low capacity of dispersion of the gold particles.

A key point when working with Au-based catalysts is that particle size and metal support interaction can be handled from the beginning of the process, namely, during the preparation of the catalyst. Various authors have claimed the importance of the preparation method over the activity of gold-based catalysts.[20,22,25] Among preparation methods the homogeneous deposition precipitation stands out since it was designed to obtain high gold dispersion with small Au particle sizes.[25] One disadvantage of this method is the use of limited specific supports, long preparation times and limited temperatures of thermal treatment. The latter is important to guarantee the catalyst stability.

In this sense, this study focuses on the design of a preparation method of bimetallic Au-Fe catalysts supported on Al_2O_3 via sequential impregnation, analyzing each operation unit involved during the synthesis. The sequential impregnation process contemplated first, the iron impregnation over alumina, and second, a stage in which gold ions species in solution could be deposited on the available surface hydroxyl groups of the support to promote well dispersion of the gold phase as well as metal-support interactions.

The variation of Au/(Au+Fe) molar ratio was investigated over the physicochemical properties and the catalytic behavior in methane combustion. Results suggests that interactions between metals and the support are promoted by shifting the Au/(Au+Fe) molar ratio, which can significantly affect the catalytic activity.

1. Experimental part

The present section contains the chemical reactants and materials used to develop the investigation. The experimental setups, characterization methods and reaction tests are also described.

1.1. Materials

Gold ore mine extract (Reina de oro, Colombian mine, Santander) was used to obtain the main metallic gold precursor. Al_2O_3 spheres (SASOL, Germany GmbH) were used as support of the catalysts. Iron (III) nitrate nonahydrate ($Fe(NO_3)_3 \cdot 9H_2O$, Merk, 99.95%) and tetrachloroauric (III) acid trihydrate ($[HAuCl_4 * 3H_2O$, Merck, 99.5%) were used as metallic precursors. Other materials used for the synthesis and characterization of the catalysts and for the methane combustion tests were: nitric acid (HNO_3, 65%), sodium chloride (NaCl, Aldrich, 99.5%), hydrochloric acid (HCl, 37%), sodium hydroxide (NaOH, 50%), sodium nitrate ($NaNO_3$, Aldrich, 99.995%), air (Linde, dry grade), nitrogen (N_2, grade 4.8 from Cryogas S.A.), argon (Ar, Cryogas S.A, grade 5.0), oxygen (O_2, Cryogas,grade 5.0), methane (CH_4, Cryogas, Grade 4.0), carbon monoxide (CO, Cryogas, Grade 4.0), and hydrogen (H_2, Linde, Grade 5.0).

1.2. Pretreatment of gold ore extract

A sample of gold ore extract was obtained from a Colombian gold mine called Mina Reina de Oro (Vetas, Santander). 1g of sample was dissolved with aqua regia to obtain a homemade tetrachloroauric acid gold precursor solution. The sample was first treated with various washes in nitric acid to purify from contaminant metals as Cu, Fe or Ag.[26] Nitric acid

is a powerful oxidant but for itself can only dissolve undetectable amounts of Au forming Au^{3+} ions. Nitric acid in presence of hydrochloric acid (aqua regia) can readily dissolve gold because of chloride ions (Cl^-) from the HCl that can react with gold ions to form tetrachloroaurate (III) anions in solution, as expressed in the following equation:[27]

$$Au + HNO_3 + 4HCl \rightleftharpoons [AuCl_4]^- + [NO] + [H_3O]^+ + H_2O$$

From the above chemistry, the second treatment of the gold sample was done with 60 mL of an aqua regia solution of HCl and HNO_3 (4:1) at 80°C. The reaction was left for about 6 hours to eliminate excess of nitric oxide and until all gold was dissolved. The resulting solution was diluted with Type I water to the desired concentration. The concentration of gold was measured by atomic absorption, as well as traces Fe, Ag and Cu. Formation of tetrachloroauric acid in this solution was verified by UV-Vis.[28,29] Additional information is reported in Appendix A.

1.3. Synthesis of catalysts

The catalysts were synthesized with a total molar concentration of metals of 10 μmol/m^2 (support) and with Au/(Au+Fe) molar ratios of 0.0, 0.025, 0.10, 0.30 and 1.00. The respective weight concentrations in terms of Au wt% were: 0.0, 0.17, 0.56, 1.20 and 2.00, keeping a total weight concentration of 2.00 wt% of the metal phase (Au+Fe).

The method of preparation of catalysts is shown in Figure 1. The method consisted on the sequential impregnation of the precursors of Fe and Au over alumina. Each unit operation involved in this process was analyzed individually starting with the wet impregnation, followed by drying and calcination (thermal treatment). The overall process is detailed below step by step.

Figure 1.

Synthesis process scheme for sequential impregnation of Au-Fe/Al$_2$O$_3$

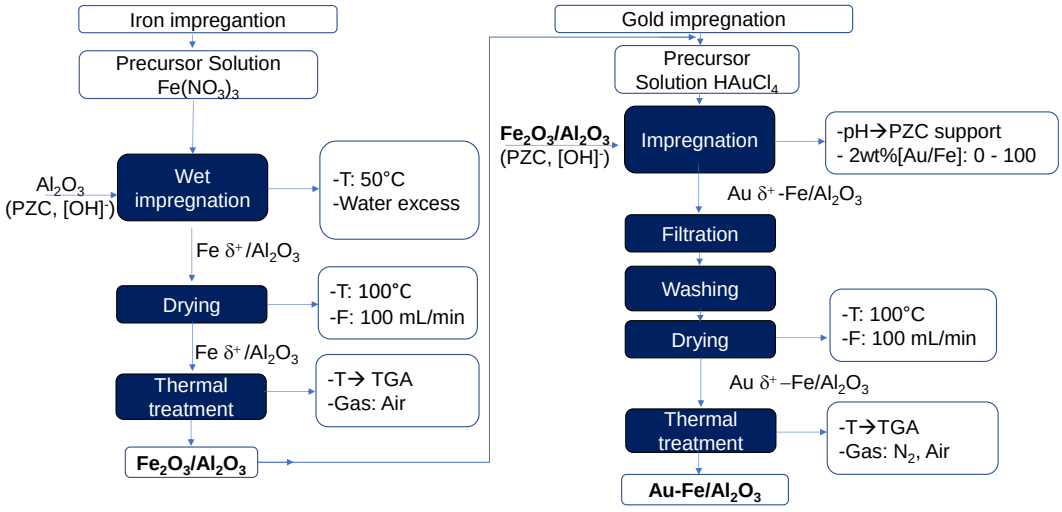

Iron impregnation

The first step of the sequential impregnation was the iron impregnation of over Al_2O_3. To carry out this process, the PZC and hydroxyl distribution of alumina was previously investigated to stablish the possibility of an electrostatic interaction between iron ions in solution with the corresponding charge of the alumina surface at the impregnation conditions. Usually, electrostatic impregnations are made changing the pH condition using an acid or a base, as required.[30] The idea here was to avoid the use of a pH modifier compound during impregnation, in order to reduce the presence of possible contaminants on the final material. In this sense, the pH of impregnation was stablished by the iron precursor solution.

The impregnation was carried out in a glass beaker of 100 mL placed in an oil bath over a heating plate, provided with a thermocouple to control the temperature. The impregnation was made by contacting the support under stirring with an aqueous solution containing the desired amount of iron precursor solution at 50°C for 1 h. To eliminate the

excess of water, the temperature was raised to 80°C until a slurry was obtained. The material was dried at 100 °C overnight. From thermogravimetric analysis, the temperature of calcination was set to 550°C, as discussed in the results section. The decomposition of the iron precursor into Fe_2O_3 with temperature has been proposed as follows:[31]

$$4[Fe(NO_3)_3 \cdot 6H_2O] \rightarrow 2Fe_2O_3 + 12HNO_3 + 18H_2O$$

Gold impregnation

During the impregnation of gold the hydrolysis of the tetrachloroauric acid was carried out. The chemistry of this process as a function of pH is as follows:[32]

$$AuCl_4^- + H_2O \leftrightarrow [AuCl_3(H_2O)] + Cl^- \leftrightarrow [AuCl_3OH]^- + H^+ + Cl^- \quad pH \approx 3 \qquad (1)$$

$$[AuCl_3OH]^- + H_2O \leftrightarrow [AuCl_2OH(H_2O)] + Cl^- \leftrightarrow [AuCl_2(OH)_2]^- + H^+ + Cl^- \quad pH \approx 4 \qquad (2)$$

$$[AuCl_2(OH)_2]^- + H_2O \leftrightarrow [AuCl(OH)_2(H_2O)] + Cl^- \leftrightarrow [AuCl(OH)_3]^- + H^+ + Cl^- \quad pH \approx 6 \qquad (3)$$

$$[AuCl_2(OH)_3]^- + H_2O \leftrightarrow [AuCl(OH)_3(H_2O)] + Cl^- \leftrightarrow [Au(OH)_4]^- + H^+ + Cl^- \quad pH \approx 7 \qquad (4)$$

According to the above chemistry, it was assumed the adsorption of gold anion species on the OH_2^+ available over the protonated alumina or Fe/Al_2O_3 surface since the preparation solution starts at acidic pH of ~3, given by the gold precursor solution. The latter was used at concentrations of ~$8x10^{-4}$ M. The solution was heated at 80 °C for 2 h, using a glass beaker of 200 mL placed in an oil bath over a heating plate, provided with a thermocouple to control the temperature. Then the desired amount of Fe/Al_2O_3 material was added. The mixture was kept under stirring at 80°C for 2 h. Finally, the mixture was washed with NH_4OH to remove residual chlorine.[33] The appropriate amount of NH_4OH was added dropwise until the pH of the solution was around 7.0 to avoid the deprotonation of the Fe/alumina surface, according to its proton affinity distribution (results section). Finally, the

material was filtered and washed with hot water several times to remove residual NH_4OH. The material was dried in an oven at 100 °C and the thermal treatment was set to 550°C, which is reported in the results section.

1.4. Materials Characterization

The properties of the Al_2O_3 support that are key for the impregnation of the metals are its point of zero charge (PZC), its distribution of surface hydroxyls, and its surface area. The point of zero charge of the Al_2O_3 and iron impregnated Al_2O_3 was determined by potentiometric titration. For the procedure, ca. 0.200 mg of Al_2O_3 were suspended in 50 mL of a NaCl solution [0.1 M]. The pH of the solution was adjusted with NaOH or HCl before suspending Al_2O_3. Suspensions were kept under stirring for 24 h and the final pH was measured. From the experimental data, a curve of pH change versus initial pH was obtained. The point of zero charge corresponded to the pH where the change of pH was zero, meaning that the total net charge of the oxides was neutral. The measurements were replicated twice.

Proton affinity distribution curves for Al_2O_3 and iron impregnated Al_2O_3 were estimated after doing continuous potentiometric titrations using a Metrohm AG instrument controlled by the TIAMO® software. For the procedure, ca. 0.200 g of Al_2O_3 were suspended in 50 mL of $NaNO_3$ solution [0.1 M]. Doses of 0.05 mL of NaOH [0.1 M] were automatically added to the suspension for the basic titration in the pH range of 7.0 to 11.0. The change in pH was recorded as a function of the added volume of NaOH. The acidic titration was made separately using HNO_3 0.1 M until a pH of ca. 3.0 to avoid the water buffer effect.[34] From the results of this test, the surface ionization constants (pK_a) and the corresponding acid-base distribution function for the solids were calculated.[35] The latter calculations, were useful to

analyze the protonation-deprotonation process of the alumina support, allowing to relate a possible interaction of charges of alumina species and species of iron and gold in solution during their respective impregnation. The protonation-deprotonation of the surface hydroxyl groups of Al_2O_3 was analyzed in terms of the surface proton concentration in acid and basic media as:[36]

$$[AlOH_2^+] \xrightarrow{K1} [AlOH][H^+] \quad (1)$$

$$[AlOH] \xrightarrow{K2} [AlO^-][H^+] \quad (2)$$

From equations 1 and 2, the equilibrium constants were considered as:

$$K_1: \frac{[AlOH][H^+]}{[AlOH_2^+]} \quad (3)$$

$$K_2: \frac{[AlO^-][H^+]}{[AlOH]} \quad (4)$$

Each dissociation step corresponds to a dissociation constant (pK_a). The pK_a values were used to build the distribution diagrams of ion surface speciation vs pH. The pK_a for the deprotonation step can be calculated from a relationship between K_1 and K_2 and considering that the pH value is equal to pK_a value when the concentration of the basic species is equal to the concentration of acid species during the dissociation,[37] i.e. $[AlO^-]=[AlOH_2^+]$. This point surges when the pH value reaches the PZC value. An approximate quantification of OH/nm^2 was calculated by the decomposition of the proton affinity distribution (PAD) curves using the software Fityk®.

The bulk contents of gold and iron on the catalysts were measured by atomic absorption. The samples were dried for 2 h at 110°C under a 100 mL/min flow of air (Linde, dry grade) before the analysis. The digestion of the samples was done using aqua regia (3HCl:

$1HNO_3$) as the digestive agent.[38] For this purpose, ca. 0.100 g of the samples were deposited on a 100 mL beaker. A solution of 50 mL of aqua regia was put in the beaker under stirring and heating at 80°C. After complete digestion, the cooled samples were diluted to 100 mL with deionized water for performing the atomic absorption test.

The porosity of the materials was assessed after measuring adsorption-desorption isotherms of molecular nitrogen at -196°C. For these measurements, samples of ca. 0.150 g of each material were weighed inside 9.00 mm diameter cells made of borosilicate glass (Micromeritics). After weighing, the cells were placed in an outgassing unit (Vac Prep 061, Micromeritics) and heated for 2 h at 300°C in order to remove adsorbed gases. The duration of the outgassing procedure was defined after finding that the vacuum in the cells reached ca. 0.05 mbar. The weight of the outgassed samples was recorded and used as input data for recording the adsorption-desorption isotherms. The adsorption-desorption isotherms for each sample were measured in a 3FLEX^{TM} (Micromeritics) instrument. Data were recorded in the relative pressure range (P/P_0) between 0.0025 and ~0.9900 using an equilibration time of 10 s. The total pore volume and the pore size distributions were calculated with the Barret-Joyner-Halenda, BJH, method[39] using the MicroActive® software provided with the instrument. However, the produced distribution can only be considered for comparison purposes since the software is restricted to pores with cylindrical geometry. In addition, the total specific surface area -SSA_{BET}- of the solids was estimated by the Brunauer-Emmett-Teller, BET, method[40]. The selection of the experimental points used for SSA_{BET} calculations was made after applying the Rouquerol transform and checking for the so-called consistency criteria.[41]

Thermogravimetric profiles of the materials were recorded with a TGA 2050 thermogravimetric balance (TA Instruments) (± 0.1 wt.% of precision). For the tests, samples were placed in a platinum sample holder and heated from 25 °C to 1000 °C, heating ramp: 10 °C/min, under a static N_2 or air atmosphere.

The reduction profiles of the catalysts were recorded using H_2 temperature programmed experiments, TPR. Tests were done in a CATLAB system coupled to a QGA mass spectrometer -MS- (Hiden Analytical). The MS was equipped with both an internal dual electron multiplier detector, SEM, and a Faraday detector, and with a precision quartz inlet heated capillary (QIC) sampling interface. Samples of ca. 0.1000 g were loaded in a quartz tube (1.0 cm i.d.) and pretreated with a 50 mL/min flow of argon at 120°C for 1h and then at 300°C for 2 h. After cooling down to 50°C, the reactor was fed with a mixture of 2 vol% H_2 in Ar (50 mL/min) while the temperature was increased at 5°C/min and up to 850°C. The consumption of hydrogen and the production of water were followed on-line with the MS. The sensitivity factors provided by the Hiden QMS library were used for quantification. The instrument was calibrated with H_2 pulses of 10μL. An approximated quantification of reduction percentage was obtained by calculating the peak area of the water signal, assuming a ratio of 1 H_2 : 1 H_2O.[42]

The dispersion of Au and Fe phases were estimated by CO and O_2 chemisorption, respectively. The measurements were made in the same CATLAB instrument described before. For the procedure, ca. 0.100 g of samples were placed inside a quartz tube (1.0 cm internal diameter) and pretreated with a 20 mL/min flow of argon at 120°C for 1h and then at 550°C for 2 h. After cooling down to 60°C, chemisorption of CO was carried out using automatic pulses of 10 μL of a gas mixture of 40% CO in Ar, controlled by the CATLAB

software. For measuring the O_2 uptake capacity of Fe surface sites, the material was additionally reduced at 300°C under 20 mL/min of 10% H_2 in Ar, purged and then the pulses of O_2 were done at the same temperature.

A total of 30 pulses were used for the measurements with equilibration time of 150 s. The signals of CO and O_2 were followed with the SEM detector. Stoichiometries were assumed of one mole of gold per mole of CO, and two moles of Fe per mol of O_2. [43,44] From these measurements, metallic particle sizes were estimated assuming hemisphere geometry and applying the following: [45]

$$D = 6\frac{(v_m / a_m)}{d_{VA}}$$

Where, $v_m$is the volume occupied by an atom m in the bulk of the metal, a_m is the surface area occupied by an atom m on a polycrystalline surface, and d_{VA} is the mean particle size. Chemisorption measurements were replicated thrice.

The morphology, chemical distribution, and crystalline structure of the metallic particles was assessed by Transmission Electron Microscopy (TEM), using a Tecnai F20 Super Twin TMP instrument. The instrument is equipped with a field emission source, resolution of 0.1 nm in 200 kV, magnificent of 1.0 MX and a GATAN US 1000XP-P camera. For energy dispersive X-ray spectrometry (EDS) analysis, an X-Max silicon drift detector from Oxford Instruments was employed. Preparation of the samples consisted of dispersing the particles of the materials in isopropanol and then applying ultrasound at room temperature, followed by deposition over a carbon-coated copper grid.

Further crystallinity analysis and crystallite particle sizes was made by X-ray diffraction (XRD). XRD measurements were performed in a BrukerD8 Advanced - Davinci diffractometer equipped with a Cu-K_α radiation source and a Lineal LynxEye detector. Diffraction patterns were recorded between $2\theta = 2.0$ and 70°, with a step time of 0.6 s which corresponds to a 2θ step of 0.02035º. From the recorded XRD patterns, average crystallite sizes (d_{XRD}) were estimated using the Scherrer equation:

$$d_{XRD} = \frac{K\lambda}{B\cos\theta}$$

Where, λ is the radiation wavelength (0.15406nm for CuKα1 radiation), 2θ, in radians, is the scattering angle selected for estimating the average crystallite size, B the integral broadening of the diffraction peak at 2θ in radians, and K a constant of ~1.18 for spherical–shaped particles.[46] The analysis of the recorded diffractograms was done with the MATCH® software.

1.5. Catalytic tests

Catalysts were tested in the methane combustion reaction. Tests were carried out in a fixed-bed quartz reactor (i.d. 1 cm) using concentric quartz tubes to properly hold the catalytic bed. Quartz wool was used to pack the catalytic bed. Reaction tests were done ramping the temperature from 500°C to 750°C and then back to 500°C using five temperature values in between. The values of the temperatures were randomly selected: 500, 550, 590, 620, 640, 730 and 750°C. A constant space velocity of 57000 mL/g*h was used under lean conditions of very diluted methane in air: 1.5% CH_4 in air.[47] Before reaction, catalysts were pretreated in-situ under 100 mL/min of N_2 at 120°C for 1 h and at 550°C for 2 h. Afterwards

they were reduced under 100 mL/min of 5% H_2 in N_2, at 300°C for 1 hour and cooled under N_2 to 200°C before feeding the reactant mixture. The reaction feed was composed of a CH_4:O_2:N_2 mixture of 3:40:150 [mL NTP -NIST definition-/min], set with mass flow controllers (Alicat). All tests were made at atmospheric pressure (~0.99 atm in Piedecuesta, Colombia). The reaction feed was analyzed at ambient temperature before and after the catalytic tests. Reaction products were analyzed using an on-line gas chromatograph -GC- (Shimadzu GC-2014ATT) equipped with both thermal conductivity and flame ionized detectors. The system was provided with a methanizer for improving the accuracy of the quantification of CO and CO_2. For the analyses, the reaction products were separated with both a HayeSep Q and a Molecular Sieve 5A column. Ar (20 mL/min) was used as carrier gas for GC analyses. The temperatures of the GC oven, the TCD, the methanizer, and FID were kept constant at 100°C, 160°C, 375°C, and 200°C, respectively. Dry air, H_2, and Ar (carrier gas) were fed to the system at 35 kPa, 65 kPa, and 60 kPa, respectively. The quantification of the reaction products was made following the methods presented elsewhere.[48] The catalytic performance of the materials was analyzed using conversions, yields, selectivity, and apparent reaction rates considering a differential reactor.

Conversion, yields, and selectivities were calculated using N_2 as internal standard following equation 5:[48]

$$X_{CH_4} = \frac{A^0_{CH_4} - A_{CH_4} * W}{A^0_{CH_4}} \quad (5)$$

Where, X refers to conversion, A_0 is the initial area of methane, and w is the ratio between the initial and final area of the N_2 standard, as read in the corresponding chromatogram: $w = \frac{A_S^0}{A_S}$.

Yields were calculated as a function of the initial moles of methane, and selectivity was expressed as a function of the total mol of products, as follows:

$$Y_p = \frac{N_p}{N_{CH_4}^0} \qquad (6)$$

$$S_p = \frac{N_p}{N_{CO_2} + N_{CO}} \qquad (7)$$

Reaction rates were estimated at methane conversions below 15% assuming differential operation of the catalytic reactor.[49] Net reaction rates ($r_{net,i}$) were estimated as moles of reactant converted per unit time per weight of catalyst (w), with the assumption that the differential plug flow reactor could be treated as a continuous stirred tank reactor (CSTR). [50] The net reaction rates were thus estimated as:

$$r_{net,i} = \frac{F_i - F_i^0}{w} \qquad (8)$$

Where, F_i^0 and F_i are the inlet and outlet molar flows, respectively, of the reactants and products. The forward CH_4 turnover rate (TOF_{f,CH_4}), was defined as the net CH_4 rate per exposed Au or Fe active site (M_{AS}) and corrected by the approach to thermodynamic equilibrium[51] ($1 - \eta_n$), described in equation 9:

$$TOF_{f,CH_4} = \frac{r_{net,CH_4}}{M_{AS}(1 - \eta_{MC})} \qquad (9)$$

Where, η_n is the approach to equilibrium parameter of the methane combustion reaction that was evaluated according to the following equation:[51]

$$\eta_{MC} = \frac{p_{CO_2} p_{H_2O}^2}{p_{CH_4} p_{O_2}^2} \frac{1}{K_{eq,MC}}$$

Where, $K_{eq,MC}$ is the reaction equilibrium constant for the methane combustion reaction at a given temperature, p_i is the average of inlet and outlet i–th compound partial pressure in the catalytic bed (atm). The equilibrium constants were estimated by performing calculations with Aspen Plus® (AspenTech) using a model for a Gibbs reactor and the Soave-Redlich-Kwong (SRK) package, since it's a method developed for hydrocarbon mixtures and light gases.[52]

Mass balances were defined as the ratio of the total mass of an atomic Z species; namely carbon, oxygen, or hydrogen, leaving the reactor to that entering it (equation 10).[48] Steady state carbon balances around 1.000 ± 0.01 (standard deviation) were achieved during all reaction tests. This suggested that the catalyst did not undergo appreciable carbon deposition during the reaction tests.

$$ZB = \frac{\sum_i N_{z,i} * F_i}{\sum_i N_{z,i} * F_i^0} \qquad (10)$$

Where, ZB represents the mass balance for a given Z species (i.e. C, O or H), and $N_{Z,i}$ the number of Z species atoms present in the i–th compound.

2. Results and Discussion

This section is divided in two main parts. The first one describes the analysis of the catalyst's synthesis by sequential impregnation, followed by the analysis of the heat treatment conditions and the physical and chemical properties studied of the catalysts. Meanwhile, the second part describes the catalytic performance of the materials prepared in the methane combustion reaction.

The nomenclature adopted for Au-Fe/Al_2O_3 catalysts was defined in terms of the Au/(Au+Fe) molar ratio as Au(X), where X is the molar ratio. The name of the support was avoided since they are all alumina supported. The metal loading used for nomenclature was the calculated by atomic absorption. Five catalysts were prepared with different Au/(Au+Fe) molar ratio of: Fe(1.00) (monometallic Fe catalyst), Au(0.02), Au(0.09), Au(0.29), and Au(1.00) (monometallic Au catalyst).

2.1. Impregnation

The main properties analyzed for sequential impregnation were the point of zero charge (PZC) and the proton affinity distribution (PAD) of the alumina. The results of these tests yielded an initial PZC value of the alumina of 7.08, which went to a value of 7.33 after iron impregnation (first step of sequential impregnation), indicating a higher pH value for neutral surface condition. Figure 2 shows the PZC curves for both Al_2O_3 and iron impregnated over Al_2O_3. As explained before, the PZC analysis was also used to estimate the ionization constants which helped to build approximated distribution diagrams of ion surface speciation vs pH for Al_2O_3, and a very ideal diagram (as guidance) of the iron supported on Al_2O_3, shown in Figure 3.

Figure 2.

pH curves for point of zero charge calculation of a) Al_2O_3 (7.08) and b) Fe- Al_2O_3 (7.33)

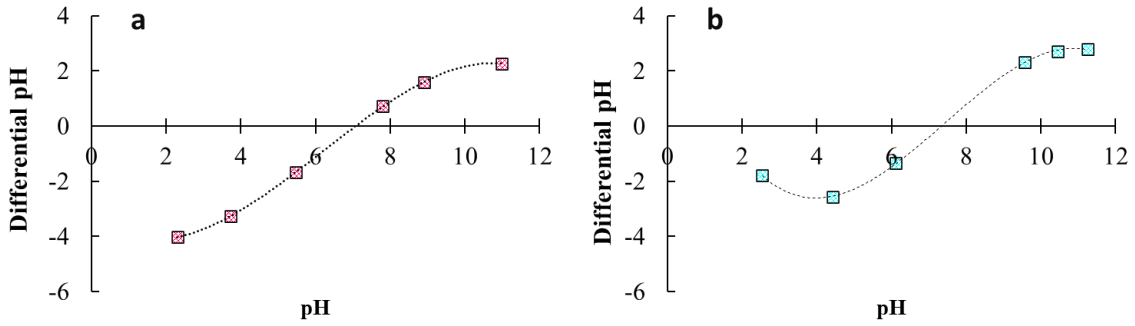

During this impregnation, the pH condition is given by the iron precursor (iron nitrate solution) with an initial pH of 2.0 ±0.3. At this pH condition, positively charged iron species would form according to both, the PZC and the Pourbaix diagram for iron.[53] Since this pH is lower than alumina's PZC, it is also positively charged. From Figure 3, it is illustrated how can be assumed that positive iron-aluminum ions coexist at pH below 4.6. In this sense, a repulsive electrostatic force generated between aluminum and iron cation species could represses agglomeration and reduce the particle size of iron oxide nanoparticles. Such phenomena has also been observed by Mosallanejad et al. [54,55], and other author used a similar explanation when reporting the formation Fe_2O_3 clusters and even isolated Fe cations on the surface of the alumina by wet impregnation.[56]

The ionization constants calculated for Al_2O_3 in solution were pK_1 = 4.3 and pK_2= 10.3, which values are similar to those reported in literature[36]. For a sample of Fe-Al_2O_3, similar constants were found, pK_1 = 4.6 and pK_2= 10.4. The pK_a values indicate the strength of an acid in solution. The lower the pK_a the stronger the acid. According to the theory of

acid-base of Lewis, an acid is an electron acceptor specie. In this case, it was considered that the low pK$_1$ value for Fe-Al$_2$O$_3$ indicated species with weak acidity.

Figure 3.

Distribution diagrams of ion surface speciation vs pH for Al$_2$O$_3$ and Fe-Al$_2$O$_3$

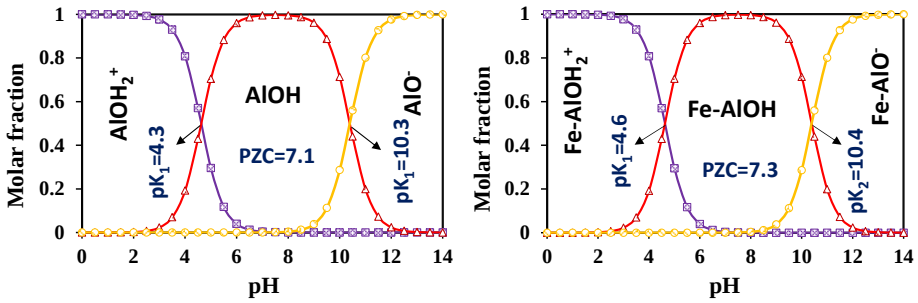

Nevertheless, these pK$_a$ values include dissolution effects that are not considered during the adsorption of basic molecules over acid solids, therefore the analysis of the behavior of species in solution must be complemented by proton affinity distribution,[54] presented in Figure 4. As can be observed in Figure 4a, for Al$_2$O$_3$ three types of hydroxyl sites could be detected. The difference between such hydroxyl groups relays on the geometry and acidity grade.[35] The observed hydroxyl groups for the tested Al$_2$O$_3$ were type IIA, IA and IB. IIA type sites are characterized for presenting intermediate acidity, double coordination regarding the OH group and tetrahedral coordination of one of the Al^{3+} cation. Sites type IA and IB present basic character, simple coordination regarding the OH group and are differenced by the tetrahedral u octahedral coordination of the Al^{3+} cation.[57] Figure 4b shows the PAD curve of Al$_2$O$_3$ impregnated with iron, and the profile of acid sites type IIA and IA increased while IB sites decreased, compared to the Al$_2$O$_3$ (Figure 4a). From the deconvolution of PAD curves, an approximate quantification of hydroxyl groups per surface

area was calculated. The OH density changed from 5.16 for Al_2O_3 to 10.4 OH/nm^2 for Fe-Al_2O_3. The change in the PAD is related to the formation of OH groups coming from the iron oxide, resulting in more prominent acid sites IIA and IA.

Figure 4.

Proton Affinity Distribution curves for Al_2O_3 before and after sequential Fe and Au impregnation.

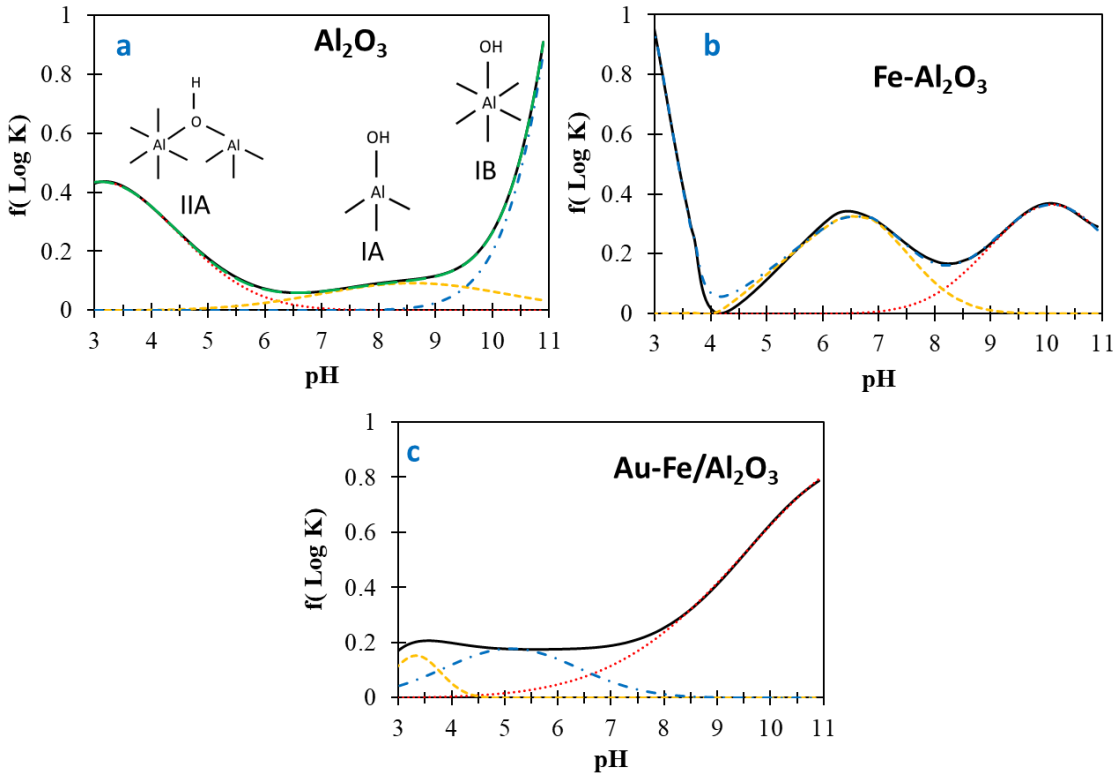

The above result is convenient for gold impregnation, as explained here. A solution of $HAuCl_4$ with an initial pH of 2.2 ±0.2 was used. Given the hydrolysis of the tetrachloroauric acid into $Au(OH)^-$ species, these anions can be anchored onto the available OH^+ of the protonated Fe-Al_2O_3 surface. Figure 4c presents the PAD for a selected Au-Fe/Al_2O_3 catalyst. It can be observed a decrement in the concentration of surface hydroxyls in the Au-Fe/Al_2O_3 as compared to Al_2O_3 and Fe-Al_2O_3. This corroborates the main

hypothesis, the presence of hydroxyl groups decreased in the pH range (8 > pH <3) of protonated and even neutral surface of Fe-Al_2O_3 after gold impregnation, traduced in a consumption of surface hydroxyl groups by gold anion species. In other words, available hydroxyl sites that were visible on the Fe-Al_2O_3 were occupied by gold species and possible gold iron mixed species. The OH density estimated for the Au-Fe/ Al_2O_3 was ca. 2.6 OH/nm^2, which corresponds to an OH species decrease of almost 76%. The explanation for the latter could be supported by literature related to adsorption of gold hydroxides over reducible oxides and the formation of gold colloids. As explained by Greffie et al.[58], two kinds of gold species were identified over iron oxides after coprecipitacion: metallic gold colloids and Au(III) species, corresponding to ca. 1- 5% of all the gold impregnated. Gold colloids formation was attributed to oxidation-reduction reactions between Au(III) and Fe(II) present as traces. They claimed that the adsorption of gold on oxidizable mineral surfaces induced the reduction of Au(III) to elemental gold, which is subsequently sorbed on oxides. In fact, colloidal gold particles are negatively surface-charged, so they can react with positively charged iron oxides by electrostatic interaction (PZC ca. 8).[59] As for the iron oxide formation here, it was confirmed by thermal decomposition analysis as discussed below.

2.2. Drying and calcination

The thermal decomposition of the impregnated materials was assessed by Thermogravimetric Analysis (TGA) in order to stablish the thermal treatment conditions. The weight losses at certain temperatures can be useful for understanding how species decompose due to the effect of the temperature and what products arise from their decomposition. Performing the analyses in air and in nitrogen also helps to understand the effect of the atmosphere composition. Figure 5 presents the TGA profiles of all samples

studied under air flow. The thermogravimetric profile of Fe(1.00) catalyst is the same of the Al_2O_3 (Appendix B). A single step weight loss below 150°C was observed, and a total weight loss of 11.3% until 800°C, corresponding to the FeO(OH) decomposition into Fe_2O_3 oxide over Al_2O_3. On the opposite, the Au(1.00) catalyst presented weight loss in two main regions, below 120°C and another ca. 300°C, corresponding to the desorption of physical adsorbed water and CO_2 and the further decomposition of gold hydroxide species into metallic gold. As gold does not form stable oxides, it can be affirmed that above 300°C only metallic gold remained.[60]

Figure 5.

Thermogravimetric profiles of alumina supported catalysts: Fe(1.00), Au(1.00), Au(0.29), Au(0.02) and Au(0.09).

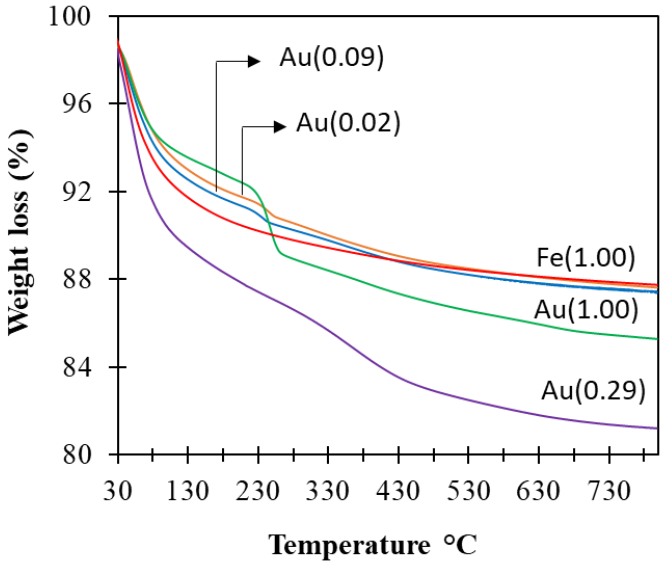

As observed in Fig. 5, the bimetallic catalysts had two weight changes that took place first around 50°C and second around 250°C, the latter being different for the catalyst Au(0.29), which second weight lost was at ca. 400°C. The first weight lost is associated to

the loss of physically adsorbed water and iron hydroxide oxidation; and the second weight loss is associated to the decomposition of the bi-metallic particles to Au + Fe_2O_3.[61,62]

The TGA analysis for a selected bimetallic Au-Fe/Al_2O_3 catalyst was also studied under N_2. The thermal profiles did not change with air or N_2 atmosphere, suggesting that the transformation of gold and iron phases does not depend on a treatment under an oxidant atmosphere. All the bimetallic catalysts showed a two steps weight change. The formation of Fe_3O_4 was discarded for bimetallic catalysts because usually the weight loss associated with the decomposition to Fe_3O_4 occurs in a single step and differs according to the atmosphere, being at 60 °C in an oxidizing atmosphere (air) or at 270 °C under N_2.[61] However, in this case the thermal profiles in air and in nitrogen were quite similar, showing the same two steps of weight loss (Appendix C).

From the analysis above, the thermal treatment for the catalysts was set to a temperature in which a constant loss weight could be observed in all samples but also cover the temperature reaction to guarantee the formed phases of Fe and Au. According to literature, temperatures higher than 400°C are not recommended to avoid agglomeration and increase of gold particle size leading to inactive gold phase.[63] In this case, all catalysts were calcined at 550°C since about this temperature a constant loss weight can be generally observed for all samples.

After calcination, the BET surface area decreased for all bimetallic catalysts (Appendix D). To study the possibility of gold and iron nanoparticles formed inside the pores of the support, the normalized surface area (N_{SABET}) of the catalysts was calculated using equation 11:[64]

$$N_{SA_{BET}} = \frac{SA_{BET_{cats}}}{(1-x)\times SA_{BET_{Al_2O_3}}} \qquad (11)$$

Where, $SA_{BET_{cats.}}$ is the BET surface area of the catalysts, and *x* is the weight fraction of metals (Au + Fe). The $N_{SA_{BET}}$ considers that values near 1.0 correspond to very well dispersed supported phases that do not present pore blocking due to nanoparticles deposition. The lower $N_{SA_{BET}}$ value of 0.80 was calculated for the Au(0.02) catalyst, which can be considered well below 1 to interpretate pore blocking after gold metal incorporation into the support[65]. Such result is consistent with the decrement observed of SA_{BET} from 205 to 170 m^2/g after gold impregnation for the catalyst Au(0.02). For the other catalysts, $N_{SA_{BET}}$ values of 0.98, very close to one, were calculated. The latter suggests the absence of pore blocking after metals incorporation into the support for the other metal molar ratios. N_2 physisorption isotherms, BJH pore size distribution and cumulative pore volume for all catalysts are included in Appendix D. Also, a statistical analysis over the observed changes in pore volume and pore size distribution suggested there were not significant differences regarding the Au/(Au+Fe) molar ratio changes, studied for the calcined materials.

In general, dispersed Au and Fe phases were generated over the support after calcination. For comparison purposes, a summary of the N_2 physisorption, PZC and PAD data for Al_2O_3, Fe(1.00) and a selected bimetallic catalyst is presented in Appendix E. A resume of the synthesis process is shown in Figure 6, according to the sequential impregnation from the chemical point of view. The influence of the formed metallic or oxide phases depending on the Au/(Au+Fe) molar ratio was assessed by TEM and XRD.

Figure 6.

Scheme representation of the main two steps of sequential impregnation.

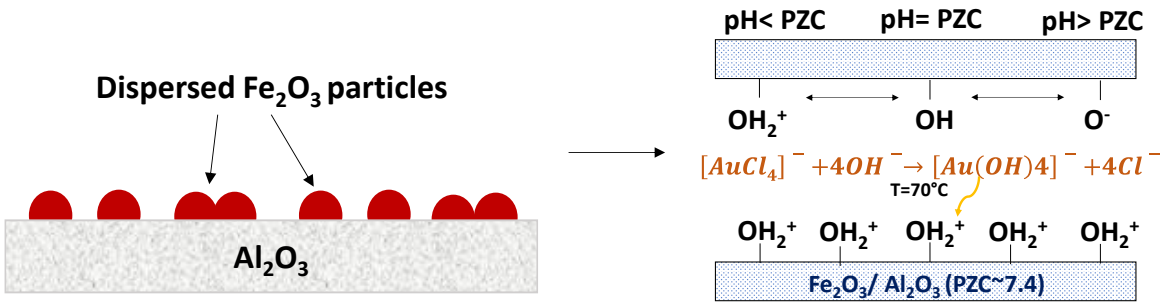

2.3. Physicochemical properties of the catalysts

TEM images for selected samples are shown in Figure 7. Chemical mapping (upper images) and particle diameter distribution assessed by Average Shifted Histograms (ASH)[66] (curve distribution images) were also included in the figure. Due to the low metallic loadings of the catalysts, the density of metallic particles was small. In the images, it can be observed that beside the presence of little dark dots, there are also dark zones corresponding to agglomeration of metal particles. For some particles, the difference between the border and the center of the particle can be distinguished, as marked in Fig 7. The rice shaped grains correspond to the Al_2O_3 support.

Nanoparticles were not distinguishable from Au or Fe in this TEM images; however, the analysis of the particle size distribution was done based on the counted particles, as showed in the ASH plots. Analyzing the chemical mapping (images at the corners), the distribution of Au and Fe particles was elucidated. The brilliant spot at the center is the electron beam and should not be confused with metal particles. Gold nanoparticles were distant from each another while iron nanoparticles are much together.

Figure 7.

TEM images including STEM for bimetallic catalysts: 1. Au(0.02), 2. Au(0.09), 3. Au(0.29), and 4. Au(1.00)

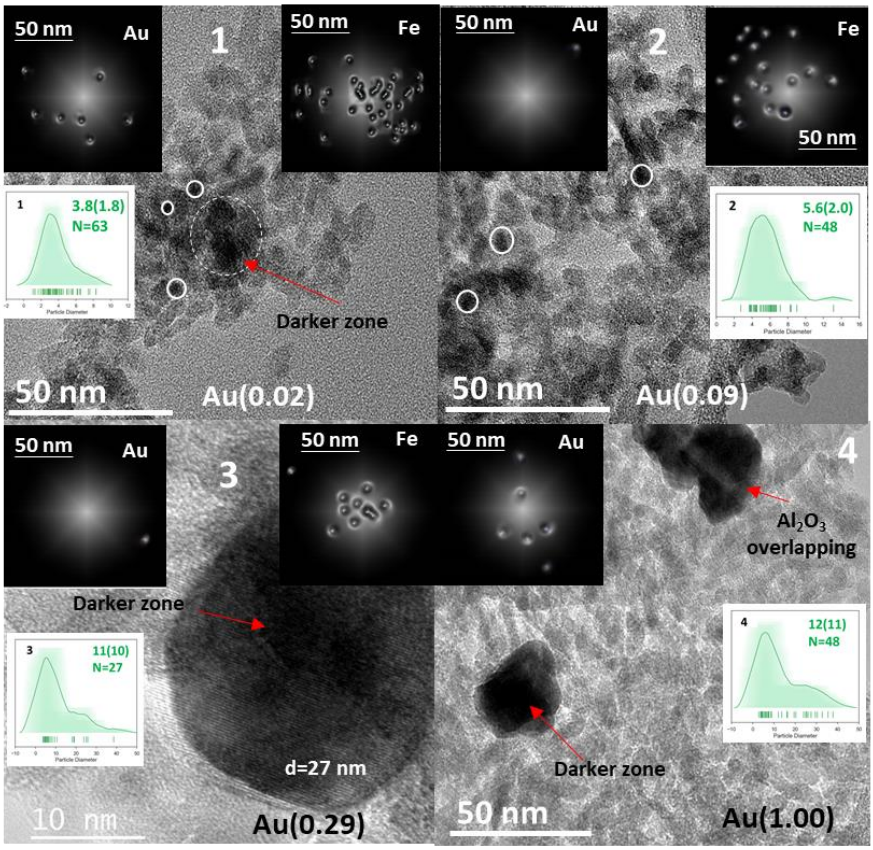

For samples with molar ratio of 0.09 and 0.29 just one Au particle seems to appear on the chemical mapping; it does not mean there is no gold but not all the present gold could be scanned due to low energy emission from the particles or even overlapping of iron particles upon the gold ones. This analysis suggests that the higher the gold loading the lower the emission. For the latter samples and also the monometallic Au(1.00) sample, the particle size distribution was very wide (ASH plots). It could be found small nanoparticles (<10 nm) and some larger particles of c.a. 40 nm. The increasing of Au particle size was attributed to Au small particles agglomeration as Au/(Au+Fe) ratio increases. As can be observed in the ASH plots integrated in Fig 7, the particle distribution tends to have a wider tail of larger

particles while increasing the metal molar ratio. It can be also attributed to agglomeration of the iron particles leading to the formation of larger iron oxide particles.

From a high-resolution TEM image of 5 nm for a selected sample of Au(0.02) (Figure 8), an isolated particle could be found (marked dark zone), with the presence of some crystalline zones determined by the patterns of parallel lines and also an amorphous zone. The hemispherical shape of the particle in Fig 8, indicates a strong interaction between the metal phase (Au+Fe) and the Al_2O_3[68], as usually found in Au/TiO_2[16,67]. This same particle was subjected to an analysis by means of an inverse Fourier Transform, which allowed determining the presence of tiny gold and iron particles around the semicircle (upper left corner image), with measured interplane distances of 2.34 Å for Au (111) and 1.78Å for Fe (101) structure. The latter was also observed by XRD (Table 1). This appreciation is related to metal particle interaction since both metals are conforming a cluster of nanometric size.

The differences between crystalline and amorphous zones in the same particle indicates a possible migration of Al_2O_3 onto the top surfaces of bimetallic nanoparticles interaction with the support[69] (Figure 7-2, 7-4 and 8). Compared to the values of interplanar distance found for Fe(101) in XRD (Table 1), for this particle (Fig. 8) is a bit higher, which suggests a kind of metal support interaction related to different coordination number of metal-oxygen of an iron metal atom in contact with the support[70]. Table 1 summarizes the identified crystalline phases in the bimetallic and monometallic catalysts with their respective Miller indices and interplanar distances calculated by XRD.

Figure 8.

TEM images, chemical mapping and EDS spectrum of a Au(0.02) sample. The left image is an analysis by Inverse Fourier Transform of a single particle.

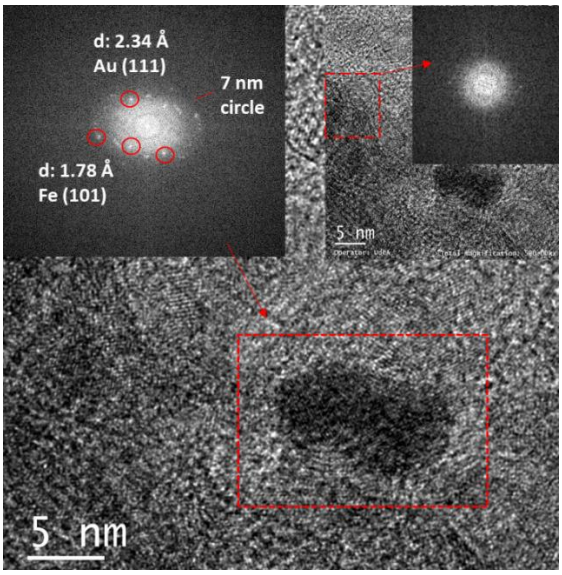

In general, Fe_2O_3 and metallic Au phases were present in all bimetallic catalysts (Table 1). Phases identification for the Au(0.02) sample was not possible to analyze with the MATCH® software due to very low metal loading. The interplanar distances (d-values) were found to be lower for bimetallic samples than monometallic ones.

Table 1.

Phases identification and interplanar distances calculated by XRD.

Catalyst	***Phase***	***%Phases***	***Planes***	***d-values(Å)***
Fe/Al$_2$O$_3$	Fe_2O_3	100	110. 214	2.50, 1.47
Au(0.02)	-	-	-	-
Au(0.09)	Au	16.4	111	2.34, 2.03
	Fe	10.7	101	1.98
	Fe_2O_3	72.9	110	2.50
Au(0.29)	Au	49.9	111, 200	2.34, 2.03
	Fe	5.2	111	2.20
	Fe_2O_3	44.9	101, 200	2.02, 1.43
Au/ Al$_2$O$_3$	Au	100	111	2.35

The contraction of interplanar distances is related to higher electron density between the atoms because of dehybridization of the spd metal orbitals and increases with decreasing gold particle crystallite[70]. Also, the Au(200) phase was observed for some bimetallic catalysts, but not for the Au(1.00) monometallic. Figure 9 shows XRD patterns for all catalysts. The broad peaks are typical of nanosized crystallites, with the objection that the metal loading is too low to observe higher intensities.

Figure 9.

XRD patterns of Au-Fe/Al2O3 catalysts with different Au/(Au+Fe) ratio, including monometallic catalysts. Samples were calcined at 550°C. (*) metallic gold, (°) γ-Al$_2$O$_3$, (#) hematite

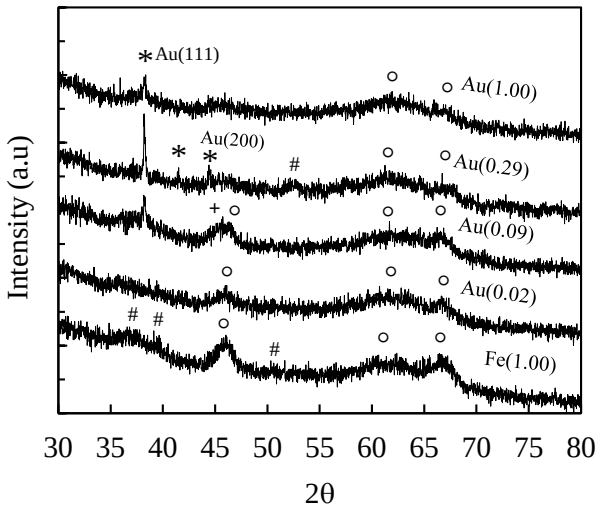

The patterns were consistent with the single-phase face centered cubic structure (fcc) for gold[71,72], with observable species of Fe_2O_3 in some samples. Increasing of iron loading affected the main gold peak Au(111) and reduced the Au(200) phase; this behavior is related to the formation of alloy compounds[71,73]. For the higher Fe catalyst content [Au(0.02)], the presence of a reflection at 67″ 2θ can be related to the γ-Al_2O_3 phase, but also because of the shape of the peak it suggests the segregation of iron with the formation of iron oxide (Fe_2O_3)[73]. In this catalyst was not possible to observe the metallic gold crystalline phase.

Given the low metal loading, it was expected higher visibility of the Al_2O_3 at its principal peaks at 45″ and 66 ″ 2θ[74]. Indeed, these peaks are visible in all samples. However, the presence of the metallic Fe can be difficult to determine visually from the given diffractogram due the close and even overlapped peaks of metallic Fe with γ-Al_2O_3, at 44″ and 65 ″ 2θ [72]. From the analysis trough the MATCH software, the presence of metallic Fe phase could be suggested for sample Au(0.09) due to the observable division of the peak at ca. 45″2θ, as presented earlier in Table 1. About the influence of the second metal in bimetallic gold based catalysts, Blosi et al. claims that increasing the increasing the amount of Cu in bimetallic Au-Cu catalysts led to polydispersed bimetallic particles with a larger mean diameter[71]. In the present case, increasing of iron loading led to the formation of smaller bimetallic particles with higher dispersion of the present gold, observed by chemisorption tests.

Table 2 summarizes the CO an O_2 chemisorption measurements with the estimated dispersion of Au and Fe. Metal surface area and dispersion were also estimated. Chemisorption technique is widely implemented to measure small nanoparticles that otherwise are not easily measure or detected.[43,75] For bimetallic catalysts it was assumed that the surface concentration of metals was the bulk concentration. The metal surface area and dispersion were calculated based on monolayer adsorption of CO and O_2 on the metal sites only. Therefore, only strong adsorbate adsorption is considered for these calculations.

Monometallic Au/Al_2O_3 was not included in Table 2 since it did not chemisorb CO or O_2. The highest dispersion of the gold phase was observed over the Au(0.02) catalyst. This result is coherent with STEM chemical mapping for this sample analyzed earlier, where the Au particles were very distant from each other.

Table 2.

Au and Fe dispersion, metal surface area and particle diameter from CO and O_2 chemisorption measurements, respectively.

	Au				***Fe***			
	Au(0.02)	***Au(0.09)***	***Au(0.29)***	***Au(1.00)***	***Au(0.02)***	***Au(0.09)***	***Au(0.29)***	***Fe(1.00)***
μmol Au or Fe/g cat	4.16 ±0.22	1.29±0.19	1.10±0.1	-	7.35 ±0.91	5.30±0.27	5.18±1.01	4.63±0.53
%Dispersion	58.62 ±3.01	4.89±0.71	2.17±0.2	-	3.33 ±0.41	3.04±0.16	5.35±1.05	2.69±0.31
Metal surface Area [m^2/g]	1.56 ±0.08	0.13 ±0.02	0.06±0.01	-	0.16 ±0.02	0.15 ±0.01	0.27±0.05	0.24±0.03
Diameter [nm]	1.99 ± 0.10	24.09 ± 3.30	53.9±4.90	-	35.37 ± 4.10	38.26 ± 1.95	22.36±5.0	43.41±5.00

Chemisorption results suggested that increasing Au content reduces the number of Au surface sites in the bimetallic Au-Fe catalysts. Dispersion and metal surface area decrease drastically with increasing gold loading. On the other hand, in terms of the Fe loading, O_2 chemisorption showed similar dispersion results among catalysts despite Au/(Au+Fe) molar ratio changes, including the monometallic Fe(1.00) catalyst. The latter had the lowest O_2 uptake compared to bimetallic catalysts, suggesting that the Au presence increases the number of iron surface sites.

Regarding the particle diameter estimations, gold particle size increases with gold loading. Figure 10 shows the statistical effect of Au or Fe mol% over the metallic dispersion in the catalysts. The dotted lines represent the upper and lower limit of the confidence interval (CI). The wide characteristic of the CI is coherent with the observed by TEM, since the particle distribution included particle sizes larger than 40 nm for the Au(0.29) sample. From Fig. 10, the lower and the higher gold loading catalysts [Au(0.02) and Au(0.29)] did not follow the tendency along the confidence interval, supporting the significant effect of the Au/(Au+Fe) molar ratio over the Au particle size. There was also a significant effect observed

for the catalyst Au(0.09), but a clear tendency of the Fe loading over the Fe particle size was not elucidated. The differences observed between Au and Fe particle sizes indicates a higher sensitivity of gold to increase as Au/(Au+Fe) molar ratio increases. A similar tendency was observed for dispersion and metal surface area (Appendix F).

Figure 10.

Statistical effect of Au/(Au+Fe) molar ratio over nanoparticle diameter measured by chemisorption.

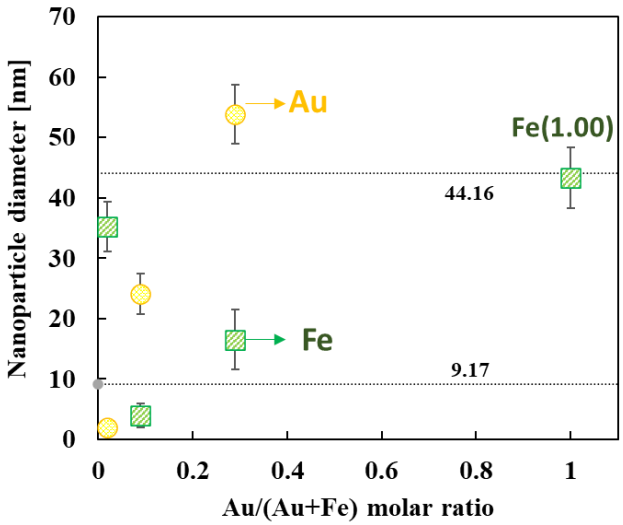

A comparison of particle sizes calculated by XRD, Chemisorption and TEM is presented in Table 3. Au particles measurements by XRD is similar to TEM measurements, except for the Au(0.29) sample which is more similar to CO chemisorption. By CO chemisorption large gold nanoparticles sizes predominated, indicating that these particles are the ones available for chemical interaction despite the presence of other smaller particles. The catalysts with the highest dispersion and smaller gold nanoparticles is the one with the lowest gold loading Au(0.02), which particle size by CO chemisorption coincides with TEM measurements.

Table 3.

Particle size comparison between XRD, Chemisorption and TEM measurements

Technique	***XRD***	***CO Chemis.***	***O_2 Chemis.***	***TEM***
Catalyst	***Au d (nm)***	***Au d (nm)***	***Fe d (nm)***	***Average (nm)***
Fe(1.00)	N.A.	N.A.	43.41 ± 5.02	-
Au(0.02)	-	1.99 ± 0.12	35.37 ± 4.11	3.8±1.84
Au(0.09)	3.23	24.09 ± 3.34	38.26 ± 1.93	5.6±2.05
Au(0.29)	64.81	53.9 ± 4.90	22.36 ± 5.10	11±9.98
Au(1.00)	7.40	-	N.A.	12±10.95

The differences in particle sizes observed by each technique were not surprising. However, there are some coincidences between them. To clarify, the average particle estimated by TEM contemplates indistinctly Au and Fe particles. In the case of Au(0.02) catalyst, it was no possible to estimate the average particle size by XRD, but CO and TEM values coincide. The latter suggests that the major particles analyzed by TEM for this samples belong to the Au metallic phase. In the other hand, for the Au(0.29) catalyst, as presented before in the ASH plots, the particle distributions estimated by TEM contemplates large particle size of ca. 60 nm despite having a lower average diameter of ca. 11 nm. For this same catalyst, the particle diameter estimated by XRD and CO chemisorption are close, but the average particle diameter calculated by O_2 chemisorption appears closer to that of TEM. In this sense, the major particles observed by TEM for this sample belong to Fe species.

The presence of Fe_2O_3 and Au was also confirmed by temperature programmed reduction analysis. This analysis can also help to elucidate the interaction between metals and the support, which is related to the degree of reducibility at higher or lower temperatures. Figure 11 shows the TPR profiles. The differences observed among bimetallic catalysts were attributed Au/(Au+Fe) molar ratio variation.

Figure 11.

Temperature programmed reduction profiles of catalysts.

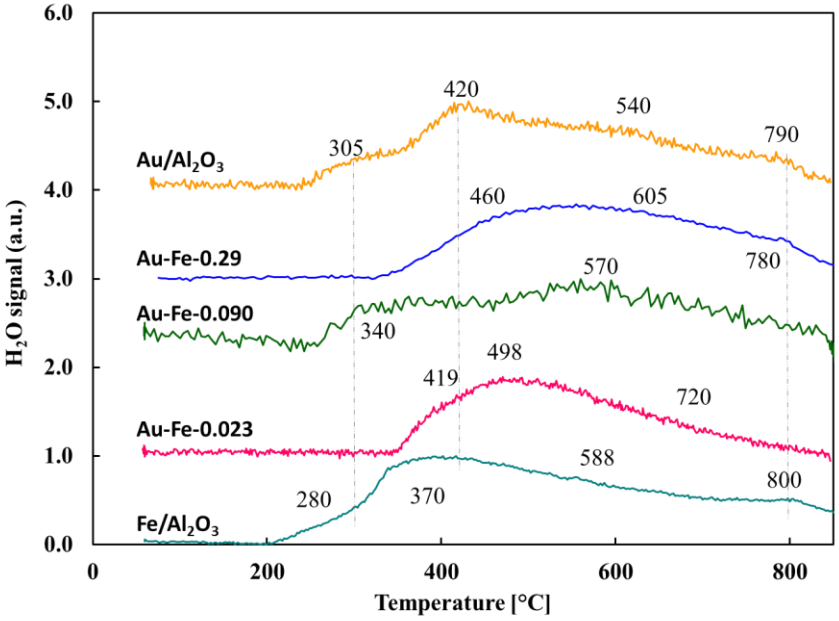

The metal loading in all the catalysts was kept below 2.00 wt%, which is why the H_2 signal during reduction steps was very poor, for this reason it was decided to analyze the water signal instead. Table 4 collects the values of hydrogen consumed at each temperature, per catalyst. From XRD and TEM analysis Au was found in its metallic state after calcination, suggesting that the reducing steps observed in TPR could be attributed to Fe oxide species transformation. The monometallic Fe(1.00) catalyst showed the lowest temperature of reduction with a distinguishable shoulder at ca. 250°C associated with transformation of Fe_2O_3 to Fe_3O_4 and posterior Fe_3O_4 to FeO at ca. 370°C, and the third region of reduction at 800°C could be associated with transformation of FeO to Fe[54]. The major H_2 consumption was observed for the Au(0.02) catalyst, which is related to the fact that this bimetallic catalyst has the higher iron loading, leading to more quantity of reduction of iron oxide species.

Table 4.

Consumed, required hydrogen and reduction percent of catalysts.

		μmol H_2/g cat	
Catalyst	***T [°C]***	***Consumed***	***Total***
Fe(1.00)	353.8	0.16	5.77
	370.2	2.40	
	588.4	2.74	
	797.6	0.48	
Au(0.02)	419.2	1.19	8.57
	498.4	3.31	
	620.9	4.07	
Au(0.09)	340.3	0.57	6.78
	569.7	6.21	
Au(0.29)	459.6	0.67	3.23
	605.1	2.17	
	778.6	0.40	
Au(1.00)	304.5	0.20	5.75
	419.0	0.80	
	540.8	4.66	
	790.2	0.10	

In general, the reduction region from 400°C to 750°C observed for all catalysts, except for the Au(1.00), can be attributed to iron oxide reduction from Fe_2O_3 to Fe_3O_4.[76,77] An increasement of the reduction temperatures was observed when increasing Au/(Au+Fe) molar ratio from 0.09 to 0.29, suggesting a stronger Fe_2O_3-Al_2O_3 interaction for the latter[78]. On the other hand, for bimetallic catalyst Au(0.02) the wide reduction steps were attributed to a strong interaction between metals and the support[79], also considering that such wide reduction peaks could be attributed to the gold nanoparticles lowering the temperature of reduction of iron oxide into metallic iron nanoparticles at temperatures above 500°C[80]. This analysis is supported with the iron species estimated by TEM and XRD above. TPR analysis helped elucidate that interactions between Au, Fe_2O_3 and Al_2O_3 strongly depend on the Au/(Au+Fe) molar ratio in the catalyst.

So far, we have found that catalysts showed bimetallic Au-Fe phases, with the presence of Fe_2O_3 and variable dispersion of the metal phases and the particle sizes. The catalysts with lower Au loading Au(0.02) presented the highest Au dispersion and lowest Au particle size as studied by CO chemisorption. The low average particle (< 4 nm) after calcination at 550°C, is interesting comparing to generally gold based catalysts studies, where recommendation is to calcine below 400°C to avoid larger particle sizes [19,22,24,63,73]

3. Catalytic performance in methane combustion

In this section, the catalysts behavior in methane combustion reaction will be discussed. Initially, a scanning of the reaction temperature was done for all samples between 500°C – 750°C. Later, the catalyst with higher activity will be discussed further to analyze its catalytic performance. Finally, stability tests and activation energy will be discussed.

Figure 12 presents the fractional conversion of methane for all catalysts in a scanning of temperature reaction from 500°C to 750°C. Catalysts showed no activity below 500°C. Under the tested conditions, both monometallic Au(1.00) and Fe(1.00) were catalytically active. The monometallic Au(1.00) had the lowest activity, even lower than the monometallic Fe(1.00). This could be related either to larger gold particles or the formation of an inactive gold-alumina phase. It was interesting that the Au(0.02) had a very similar behavior to the Au(0.09) catalyst, and both catalysts showed higher catalytic activity than Fe(1.00) monometallic catalyst. The latter suggest that the bimetallic particles found in the bimetallic catalysts improved the catalytic performance compared to the iron activity. One thing is clear, in all catalysts the formation of an active iron phase was achieved since the monometallic Fe(1.00) catalyst was also active. Even though there are discrepancies in literature about iron

catalysts activity in methane, this result is coherent with some resports[81]. In summary, the gold presence improved the catalytic activity when Au/(Au+Fe) molar ratios where below 0.09.

Figure 12.

*Catalytic behavior of Au-Fe/Al$_2$O$_3$ catalysts in methane combustion at different temperatures. GHV: 57000 mL/g*h*

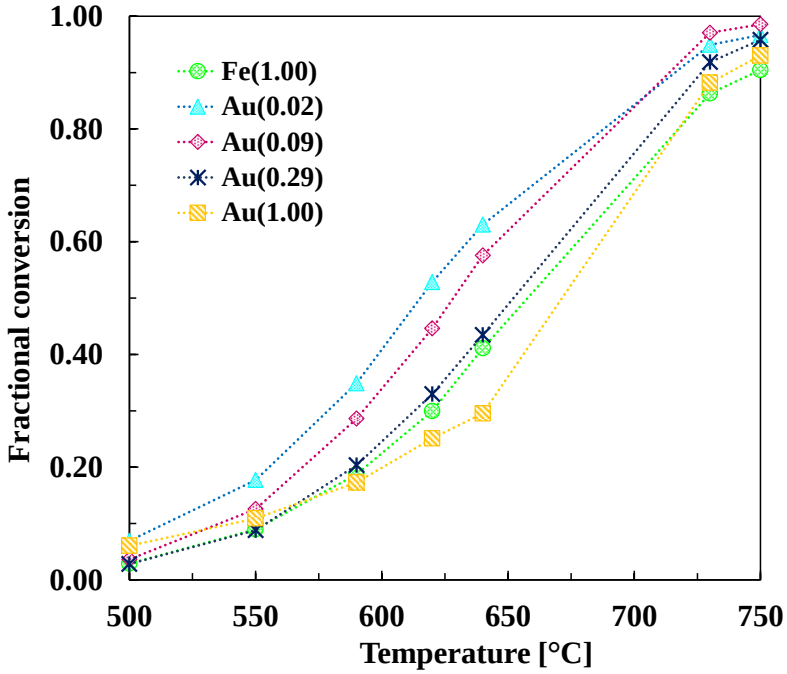

The highest activity observed in terms of methane conversion was obtained with the catalyst with lowest gold content Au(0.02). The results showing the temperature required for methane conversions of 10, 50 and 90 are presented in Table 5. As discussed earlier, the catalyst Au(0.02) presented the higher dispersion and lower particle size, so it is coherent that this same catalysts showed lower temperatures for required conversions.

Table 5.

Temperatures required for different methane conversions over Au-Fe/Al$_2$O$_3$ catalysts varying Au/(Au+Fe) molar ratio.

	T[°C] for required CH$_4$ conversion		
Catalyst	**T^{10}**	**T^{50}**	**T^{90}**
Fe(1.00)	550	660	750
Au(0.02)	512	620	715
Au(0.09)	545	630	718
Au(0.29)	550	650	725
Au(1.00)	550	670	735

The variation of gold content over the methane conversion is presented in Figure 13 for temperatures below 640°C, aiming to compare the decreasing observed in methane conversion while increasing Au mol% loading in the catalysts. The effect of temperature was also marked in the figure.

Figure 13.

Effect of Au mol% in catalysts over the methane fractional conversion. Temperatures for such conversion are pointed out.

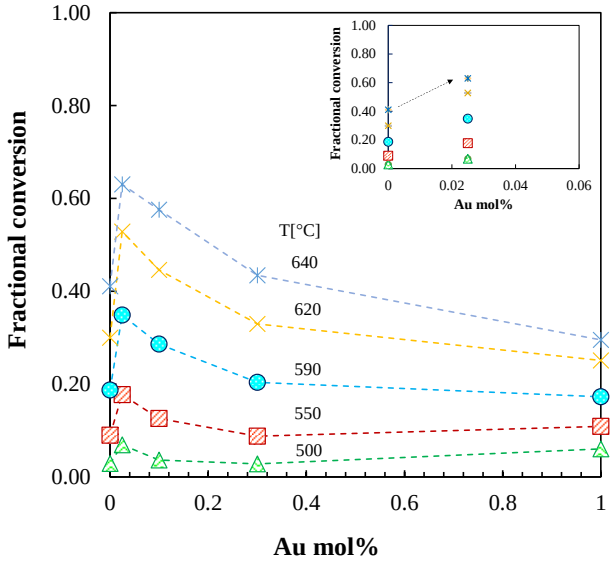

The zoomed image presented at the corner of Figure 13 points out the increment in catalytic methane conversion from Fe(1.00) monometallic to Au(0.02) bimetallic catalyst. Catalytic results confirmed the inverse relation between gold content and activity in methane combustion, so that the minor the gold content in the catalysts, the greater the catalytic activity. This is in agreement with reported in literature by Hutchings et al[82].

As mentioned earlier all catalysts were evaluated during ignition and extinction between 500 to 750°C. The ignition-extinction reaction graphics for all catalysts are presented in Appendix G. The performance of catalysts in reaction during ignition-extinction experiments can present basically two types of hysteresis: normal, if the catalytic activity increases during extinction, or reverse, if the catalytic activity decreases during extinction[83]. In this case, all the catalysts exhibited inverse hysteresis. This behavior could be related to the formation of a less active catalytic phase of Au-Fe during reaction, which could well be due to the oxidation of initially metallic Fe particles. The inverse hysteresis is also usually related to the size of the noble metallic nanoparticles as in the case of Pt. For CO oxidation, when the Pt particles are smaller than 2 nm, an inverse hysteresis occurs. However, the opposite behavior was observed for gold, since lower gold particle sizes decrease the inverse hysteresis phenomenon tending to change from inverse hysteresis to normal hysteresis. In this case, the inverse hysteresis could also be affected by the growth of the gold nanoparticles during the extinction process.

To study the reaction in the kinetic region, the catalysts Au(0.02) was selected and tested at temperatures below 550°C to obtain methane conversions lowers than 15%. The randomly selected temperatures were 500, 518, 523 and 536 °C. The activity was evaluated

during ignition and extinction. A decrease of about 3% in the methane conversion was detected (Figure 14). The values in the graphic include error bars for the average of the conversion measurements at each temperature, using a student's t-test with a 95% confidence interval. As expected, the activity of the catalyst increases with temperature, and decreases during extinction. The methane conversion at 500 °C differs by 3% from the final value taken during extinction. Regarding the oxygen conversion, this was kept below 4% throughout the process. Selectivity towards CO_2 was ca. 0.99 (Figure 11), and traces of CO product of incomplete combustion were observed.

Figure 14.

Catalytic behavior of Au(0.02) on methane combustion reaction at different temperatures between 500 and 536 °C, for ignition and extinction process.

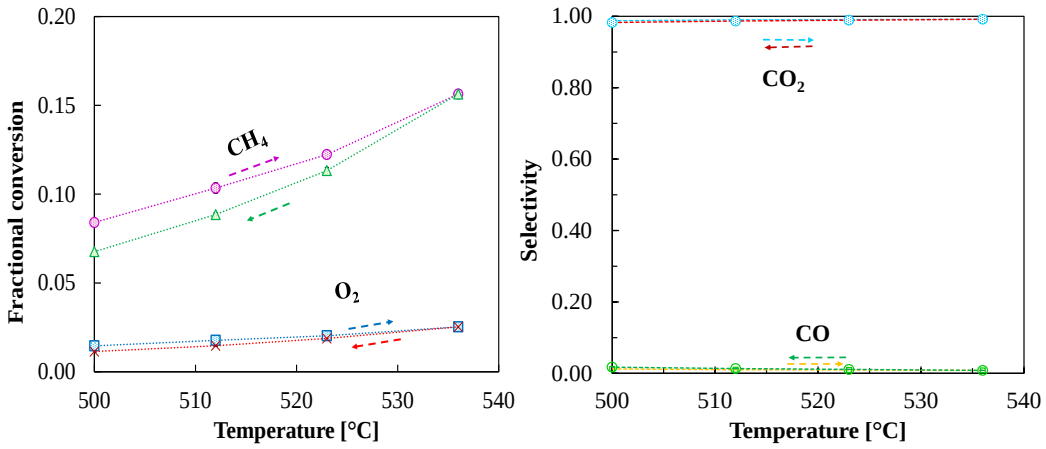

For Au-based catalysts generally a reduction pretreatment under hydrogen is implemented to ensure the formation of the metallic Au or the reduction of an oxide phase present in the catalyst[22]. It is well accepted that the former activation step could favor the formation of defective centers upon the material on which reactive O_2^- surface species would

form[84]. This explanation has been brought up not only because of Au phase but because of the presence of Fe_2O_3 in the catalyst.

However, in this study it was observed that the reduction process prior to the reaction does not affect the catalytic performance. Figure 15 presents the activity results of Au(0.02) in terms of methane conversion compared with and without catalyst's previous reduction. This comparison suggests that no previous reduction process is needed, therefore the active phase in the catalysts is formed before during thermal treatment. This also suggested that the formed reduced phases observed during TPR do not affect or participate in these catalysts during methane combustion reaction.

Figure 15.

Activity comparison of Au(0.02): a) unreduced and b) reduced, in reaction at temperatures between 500°C-550°C.

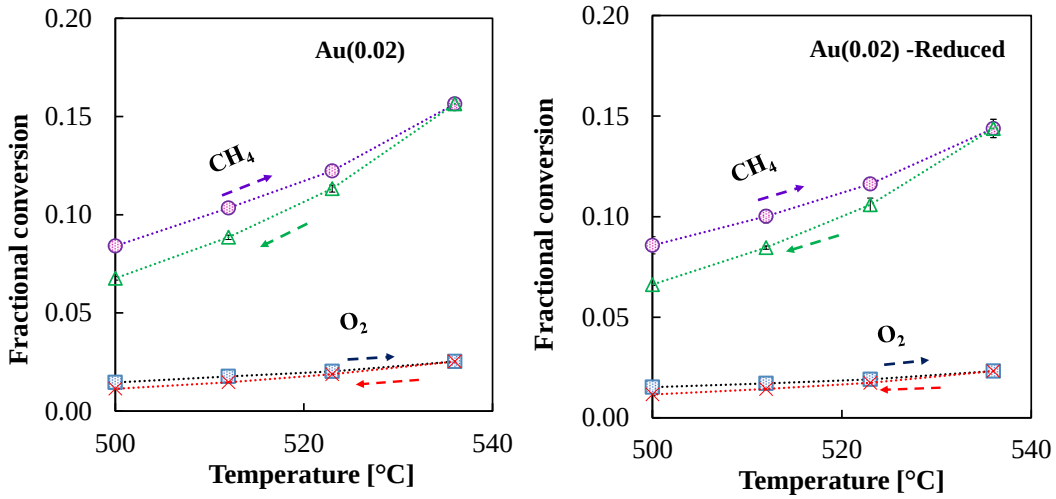

To study the active phase, the forward reaction rate in terms of TOF was calculated per exposed surface metal active sites estimated by chemisorption (Figure 16). From non-reducible ("inert") supports as Al_2O_3, low assistance during methane activation for the

oxidation reaction is expected, and reaction is supposed to proceed only over the active composed by Au+Fe sites where CH_4 and O_2 can be absorbed, with the assistance of the present Fe_2O_3 particles as observed by TEM and XRD results. The Fe_2O_3 is generally considered as an accurate phase for the O_2 activation step due its redox ability. The difficult step of O_2 activation has also been studied over small Au particles (ca. 2nm)[84,85] which is close to the Au particle size measured for Au(0.02) catalyst by CO chemisorption. Other authors that studied Au/Al_2O_3 catalysts proposed a mechanism involving Au^+ cation carrying on OH^- group have been proposed, attributing the active site to an Au^+-OH^- ensemble in company of Au^0 atoms[86]. Since Au oxide species were not observed in this study, this reaction mechanism is not further discussed.

Figure 16.

Forward reaction rates in terms of Au or Au+Fe surface metallic phases estimated by chemisorption.

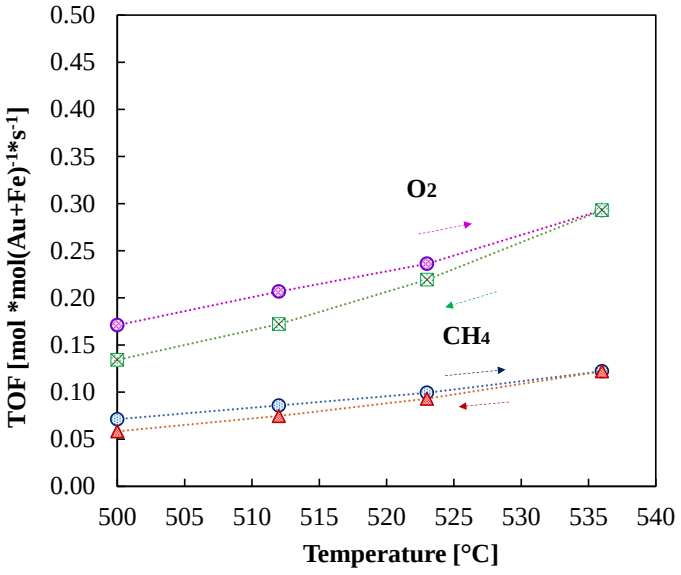

The forward reaction rates analyzed from Figure 16 showed O_2 TOF values twice higher than CH_4 per exposed bimetallic active sites, indicating complete methane combustion following the stoichiometry of the reaction. Also, considering that the uptake capacity of the

Au phase measured by chemisorption was always higher than the Fe phase in all catalysts, the increase in reaction rate with temperature for both CH_4 and O_2, is assumed to be related more to Au sites than to Fe sites. On the other hand, the higher activity observed for the lowest gold loading catalysts could indicate that the Fe phase was the major active phase in reaction. However, the results suggested that is not the lower gold loading but the lower Au/(Au+Fe) molar ratio that favors the formation of smaller gold nanoparticles that in contact with the iron species led to a more active catalytic phase conformed by bimetallic particles. The latter is related to a synergistic effect between Au and Fe at small Au/(Au+Fe) molar ratio.

The general decrease in catalytic activity observed in reaction was attributed to an increase in metal particle sizes, as observed by a TEM image of a spent Au(0.02) catalyst (Figure 17). The average particle size changed from 3.8 +/- 1.8 nm to 6.2 +/-1.5 nm, confirming that little particle changes in the range of 2.4 nm significantly affect the stability of the catalyst.

Figure 17.

TEM image of a spent sample of Au(0.02) after ignition – extinction reaction between 500°C – 536°C.

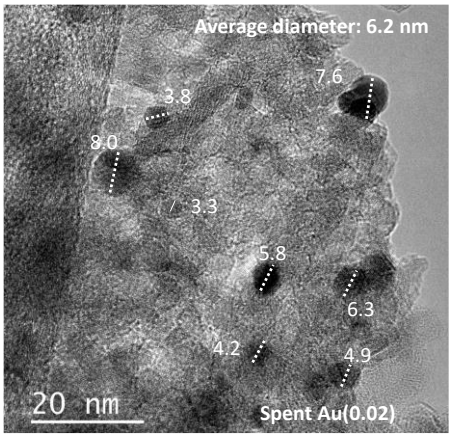

Also, the CO chemisorption test for this sample showed Au metallic surface dispersion of 20%, which is a 30% lower dispersion comparing to fresh catalyst dispersion showed earlier (Table 2). For comparison purposes another catalyst Au(0.02) was synthesized trough the same sequential impregnation using a commercial salt gold precursor $HAuCl_4$. The comparison is shown in Figure 18. These results suggests that the catalyst synthesized here (Fig 18a) could achieve better catalytic activity despite the origin of the gold precursor.

Figure 18.

Comparison of fractional conversions for Au(0.02) catalyst synthesized with different gold precursor: a) homemade $HAuCl_4$ disolution prepared in the laboratory and b) commercial $HAuCl_4$ disolution.

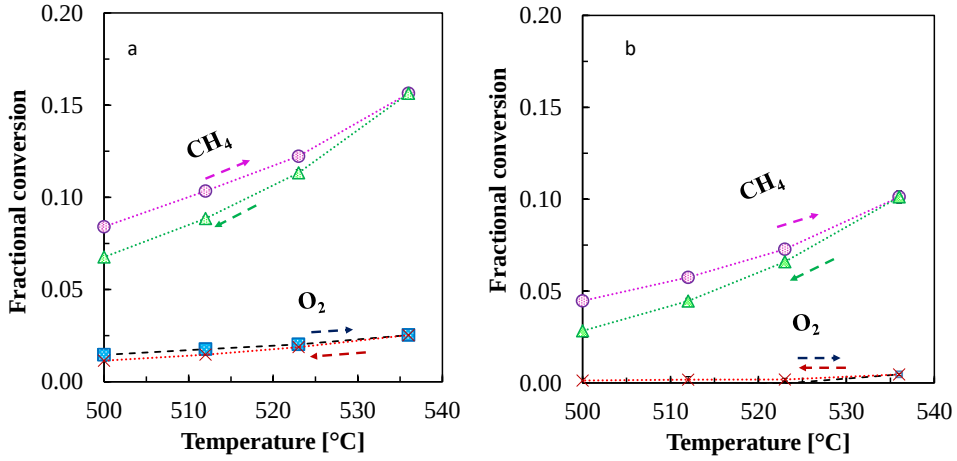

About the stability, it is common to find in literature that gold-based catalysts are not very stable over time, primary due to gold particles agglomeration, size increasing and further deactivation, even more at temperatures above 400°C. Therefore, to elucidate the stability of the synthesized catalysts, stabilization tests were made using the same reaction conditions describe earlier. The tests were carried out at 3 temperatures of 500 °C, 518 °C and 536 °C.

The stability test for the latter temperature is shown in Figure 19. The other stability tests are shown in Appendix H. The mass carbon balance is also included in Figure 19 (red dotted line above).

Figure 19.

*Au(0.02) stability test at 536 °C [57000 mL/g*h was used under lean conditions of 1.5% CH_4 in air]*

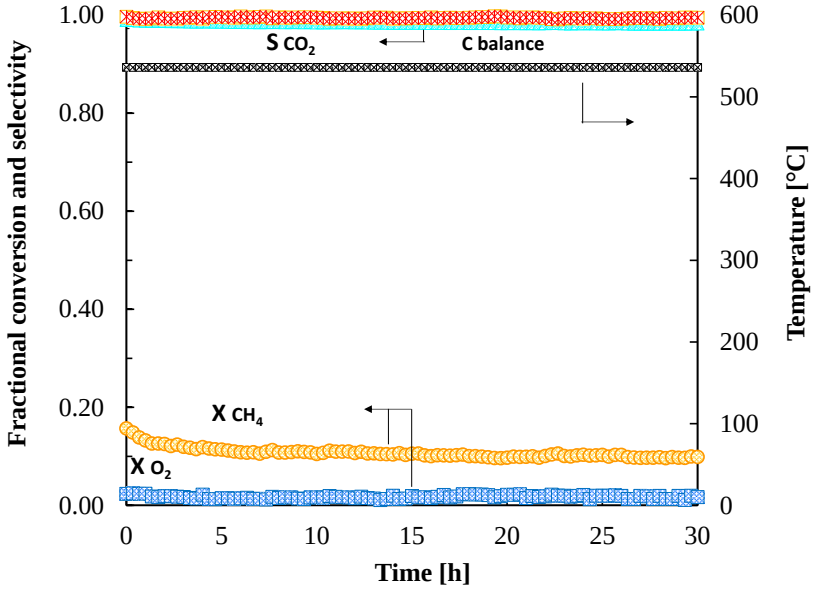

It was observed a change in stability within 5 hours. Later, a slight change of stability over time takes place until finally, the constant stability is achieved after ca. 8 hours, with a 5% decrease in methane conversion. The stability tests were used to estimate the apparent activation energy of the catalysts within the stable region data of methane conversion. The former analysis was made using Arrhenius plots, presented in Figure 20, showing the apparent activation energies of 100 kJ/mol for CH_4 and 110 kJ/mol for O_2. These values were found to be approximated to those reported in literature for gold based catalysts.[20,87]

From the analysis made so far, it was decided to make further investigation lowering the metal molar ratio to half the ratio of the best ratio studied earlier i.e. Au(0.02), obtaining an Au(0.01) catalyst. The results for the latter were very surprising since a normal hysteresis was observed after a catalytic activation at ca. 520°C. Figure 21 presents the normal hysteresis observed in terms of methane and oxygen conversion. Three replicates of this catalyst in reaction confirmed the observed behavior.

Figure 20.

Arrhenius plot for Au(0.02) with data from stability tests results for a) CH_4 and b) O_2

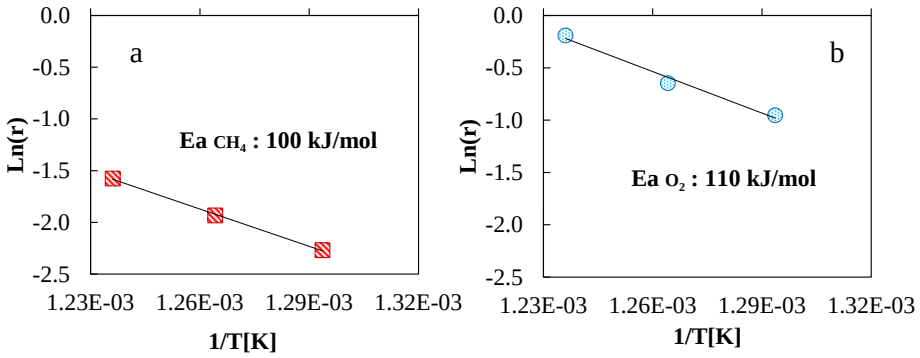

Figure 21.

Catalytic performance of Au(0.01)

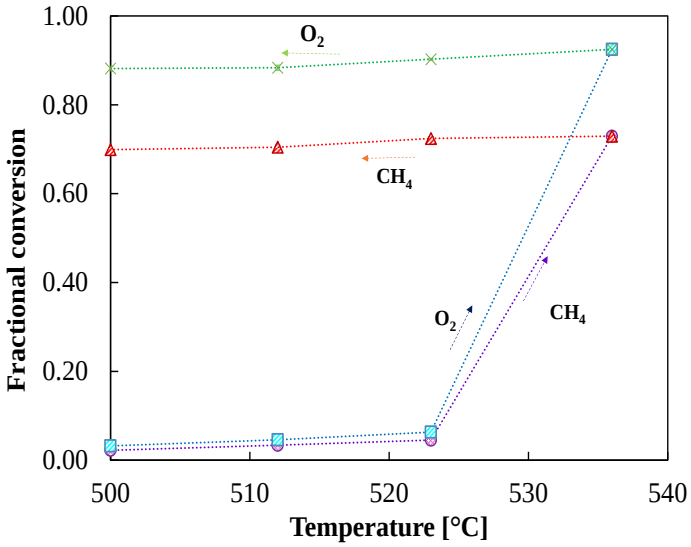

The ignition of the catalyst is given during ramping up temperature above ca. 520 °C achieving methane and oxygen conversions of 70% and 90%, respectively, which remains constant even during the extinction (normal hysteresis). Also, beside CO_2 and CO, H_2 was observed in the product current. The dispersion of the Au metallic phase calculated by CO chemisorption test for this catalyst was ca. 90%. The latter agrees with the previous assumption about increasing Au dispersion with lowering Au/(Au+Fe) molar ratio. Also, the average diameter estimated by the CO uptake capacity was lower than 2 nm (ca. 1.29 nm).

Clearly, Au dispersion and particle diameter are directly proportional, and can be promoted with lower Au/(Au+Fe) molar ratios. There are not studies in literature that report the hysteresis behavior of gold-based catalysts in methane combustion observed here. Therefore, these findings are very promising in catalysis field. The latter result requires a more extended investigation that is being carry out, but extra limits the scope of the project.

4. Conclusions

The sequential impregnation method implemented for catalysts preparation led to the formation of bimetallic Au-Fe catalysts, with the presence of Fe_2O_3 phase. The analysis of thermal treatment along with XRD and TEM confirmed the formation of iron oxide species and an Au-Fe alloy was elucidated. Results suggested that metal support interaction was stronger for the catalyst with the lowest gold loading, since an Al_2O_3 overlapping Au-Fe bimetallic particles was observed by TEM.

Catalytic results showed that the reduction activation step prior to reaction did not affect the catalytic activity, indicating that the active species of Au and Fe phases were formed during calcination. This was supported with TPR analysis since reduced iron species were observed, but according to catalytic findings, such species would not take place in reaction. The selectivity was found to be ca. 1.00 for CO_2 indicating complete methane combustion.

Lowering the Au/(Au+Fe) ratio improved the activity in methane combustion. The latter was related to higher dispersion and lower Au particle sizes always in presence of Fe. This result was confirmed with testing an ultimate synthesized catalyst with lower Au/(Au+Fe) molar ratio of 0.01, suggesting synergistic behavior between the bimetallic phase at such lower molar ratios.

References

1. Ismail, O. S. & Umukoro, G. E. Global Impact of Gas Flaring. *Energy Power Eng.* **04**, 290–302 (2012).

2. Ajugwo, A. O. Negative Effects of Gas Flaring: The Nigerian Experience. *J. Environ. Pollut. Hum. Heal.* **1**, 6–8 (2013).

3. van der Vaart, D. R., Vatvuk, W. M. & Wehe, A. H. Thermal and Catalytic Incinerators for the Control of VOCs. *J. Air Waste Manage. Assoc.* **41**, 92–98 (1991).

4. Lee, J. H. & Trimm, D. L. Catalytic combustion of methane. *Fuel Process. Technol.* **42**, 339–359 (1995).

5. He, C. *et al.* Recent Advances in the Catalytic Oxidation of Volatile Organic Compounds: A Review Based on Pollutant Sorts and Sources. *Chem. Rev.* **119**, 4471–4568 (2019).

6. Thevenin, P. Catalytic combustion of methane. (Kungliga Tekniska Hogskolan, 2002). doi:10.1080/00102209608935587.

7. Li, Z. & Hoflund, G. B. A Review on Complete Oxidation of Methane at Low Temperatures. *J. Nat. Gas Chem.* **12**, 153–160 (2003).

8. Li, X. *et al.* 3DOM LaMnAl11O19-supported AuPd alloy nanoparticles: Highly active catalysts for methane combustion in a continuous-flow microreactor. *Catal. Today* **308**, 71–80 (2018).

9. Kamiuchi, N. & Eguchi, K. Catalytic combustion of methane. *Catalysis for Alternative Energy Generation* vol. 9781461403 305–327 (2012).

10. Choudhary, T. V., Banerjee, S. & Choudhary, V. R. Catalysts for combustion of methane and lower alkanes. *Appl. Catal. A Gen.* **234**, 1–23 (2002).

11. Scirè, S. & Liotta, L. F. Supported gold catalysts for the total oxidation of volatile organic compounds. *Appl. Catal. B Environ.* **125**, 222–246 (2012).

12. Xu, H., Li, Y., Luo, X., Xu, Z. & Ge, J. Monodispersed gold nanoparticles supported on a zirconium-based porous metal-organic framework and their high catalytic ability for the reverse water-gas shift reaction. *Chem. Commun.* **53**, 7953–7956 (2017).

13. Haruta, M. Size- and support-dependency in the catalysis of gold. *Catal. Today* **36**, 153–166 (1997).

14. Tabakova, T. *et al.* CO and VOCs Catalytic Oxidation Over Alumina Supported Cu–Mn Catalysts: Effect of Au or Ag Deposition. *Top. Catal.* **60**, 110–122 (2017).

15. Bond, G. C. & Thompson, D. T. Catalysis by Gold. *Catal. Rev. - Sci. Eng.* **41**, 319–388 (1999).

16. Haruta, M. Catalysis of gold nanoparticles deposited on metal oxides. *Cattech* **6**, 102–115

(2002).

17. Zanella, R. Síntesis de catalizadores bimetálicos Au-Sn / TiO 2 y su aplicación en la reacción de oxidación de CO * Synthesis of Au-Sn / TiO 2 bimetallic catalysts and their application in the oxidation reaction of CO. **12**, 41–61 (2019).

18. Fang, Y.-L. *et al.* Structural analysis of palladium-decorated gold nanoparticles as colloidal bimetallic catalysts. *Catal. Today* **160**, 96–102 (2011).

19. Ferouani, G., Ameur, N. & Bachir, R. Preparation and characterization of supported bimetallic gold–iron nanoparticles, and its potential for heterogeneous catalysis. *Res. Chem. Intermed.* **46**, 1373–1387 (2020).

20. Grisel, R. J. H. & Nieuwenhuys, B. E. Comparative study of the oxidation of CO and CH4 over Au/MOx/Al2O3 catalysts. *Catal. Today* **64**, 69–81 (2001).

21. Grisel, R. J. H., Kooyman, P. J. & Nieuwenhuys, B. E. Influence of the preparation of Au/Al2O3 on CH4 oxidation activity. *J. Catal.* **191**, 430–437 (2000).

22. Choudhary, V. R., Patil, V. P., Jana, P. & Uphade, B. S. Nano-gold supported on Fe2O3: A highly active catalyst for low temperature oxidative destruction of methane green house gas from exhaust/waste gases. *Appl. Catal. A Gen.* **350**, 186–190 (2008).

23. Haruta, M. Novel catalysis of gold deposited on metal oxides. *Catal. Surv. from Japan* **1**, 61–73 (1997).

24. Ilieva, L. *et al.* Alumina supported Au/Y-doped ceria catalysts for pure hydrogen production via PROX. *Int. J. Hydrogen Energy* 233–245 (2019) doi:10.1016/j.ijhydene.2018.03.005.

25. Vigneron, F. & Caps, V. Evolution des méthodes chimiques de préparation des catalyseurs d'oxydation à l'or. *Comptes Rendus Chim.* **19**, 192–198 (2016).

26. Celep, O., Yazici, E. Y. & Deveci, H. A Preliminary Study on Nitric Acid Pre-treatment of Refractory Gold/Silver Ores. *Proc. 25th Int. Min. Congr. Exhib. Turkey* 11–14 (2017).

27. Elomaa, H. *et al.* The effect of the redox potential of aqua regia and temperature on the Au, Cu, and Fe dissolution from WPCBs. *Recycling* **2**, (2017).

28. Usher, A., McPhail, D. C. & Brugger, J. A spectrophotometric study of aqueous Au(III) halide-hydroxide complexes at 25-80 °C. *Geochim. Cosmochim. Acta* **73**, 3359–3380 (2009).

29. Gross, S. Colloidal dispersion of gold nanoparticles. in *Materials Syntheses: A Practical Guide* (2008). doi:10.1007/978-3-211-75125-1_21.

30. Regalbuto, J. R. Electrostatic Adsorption. in *Synthesis of Solid Catalysts* (2009). doi:10.1002/9783527626854.ch3.

31. Melnikov, P., Nascimento, V., Arkhangelsky, I. & Consolo, L. Thermal decomposition mechanism of iron(III) nitrate and characterization of intermediate products by the technique of computerized modeling. *J. Therm. Anal. Calorim.* **111**, (2014).

32. Moreau, F., Bond, G. C. & Taylor, A. O. Gold on titania catalysts for the oxidation of carbon monoxide : control of pH during preparation with various gold contents. *J. Catal.* **231**, 105–114 (2005).

33. Ivanova, S., Petit, C. & Pitchon, V. Application of heterogeneous gold catalysis with increased durability: Oxidation of CO and hydrocarbons at low temperature. *Gold Bull.* **39**, 3–8 (2006).

34. Pérez-Martínez D. de J., Acevedo-Quiroga G. A., Giraldo-Duarte S. A., & C.-H. A. Surface characterization of borated γ-alumina by using proton affinity distributions. *Rev. Fac. Ing. Univ. Antioquia* **57**, 23–30 (2013).

35. Contescu, C., Jagiello, J. & Schwarz, J. A. Proton affinity distributions: A scientific basis for the design and construction of supported metal catalysts. *Stud. Surf. Sci. Catal.* **91**, 237–252 (1995).

36. Hao, X., Spieker, W. A. & Regalbuto, J. R. A further simplification of the revised physical adsorption (RPA) model. *J. Colloid Interface Sci.* **267**, 259–264 (2003).

37. Regalbuto, J. *Catalyst Preparation: Science and Engineering*. *Focus on Catalysts* vol. 2007 (2007).

38. Garcia, M. A. S., Silvestre, D. M., Nomura, C. S. & Rossi, L. M. Determination of metal loading in heterogeneous catalyst by slurry sampling flame atomic absorption spectrometry. *J. Braz. Chem. Soc.* **26**, 359–364 (2015).

39. Barrett, E. P., Joyner, L. G. & Halenda, P. P. The Determination of Pore Volume and Area Distributions in Porous Substances. I. Computations from Nitrogen Isotherms. *J. Am. Chem. Soc.* **73**, 373–380 (1951).

40. Brunauer, S., Emmett, P. H. & Teller, E. Adsorption of Gases in Multimolecular Layers. *J. Am. Chem. Soc.* **60**, 309–319 (1938).

41. Rouquerol, J., Llewellyn, P. & Rouquerol, F. Is the BET equation applicable to microporous adsorbents? *Stud. Surf. Sci. Catal.* **160**, 49–56 (2007).

42. Wendel, J., Manchili, S. K., Hryha, E. & Nyborg, L. Oxide reduction and oxygen removal in water-atomized iron powder: a kinetic study. *J. Therm. Anal. Calorim.* **142**, 309–320 (2020).

43. Prati, L. & Villa, A. *Gold catalysis: Preparation, characterization and applications*. *Gold Catalysis: Preparation, Characterization and Applications* (2015). doi:10.4032/9789814669290.

44. Fadoni, M. & Lucarelli, L. Temperature programmed desorption, reduction, oxidation and flow chemisorption for the characterisation of heterogeneous catalysts. Theoretical aspects, instrumentation and applications. *Stud. Surf. Sci. Catal.* **120 A**, 177–225 (1999).

45. Bergeret, G. & Gallezot, P. Particle Size and Dispersion Measurements. in *Handbook of Heterogeneous Catalysis* 738–765 (2008). doi:10.1002/9783527610044.hetcat0038.

46. Valério, A. & Morelhão, S. L. Usage of Scherrer's formula in X-ray diffraction analysis of

size distribution in systems of monocrystalline nanoparticles. 1–9 (2019).

47. Machin, N. E., Caklrca, E. E. & Ates, A. Catalytic combustion of methane. in *6th International Advanced Technologies Symposium (IATS'111)* (2011).

48. Sandoval-Bohorquez, V. S., Rozo, E. A. V. & Baldovino-Medrano, V. G. A method for the highly accurate quantification of gas streams by on-line chromatography. *J. Chromatogr. A* **1626**, 461355 (2020).

49. Ajmera, S. K., Delattre, C., Schmidt, M. A. & Jensen, K. F. Microfabricated differential reactor for heterogeneous gas phase catalyst testing. *J. Catal.* **209**, 401–412 (2002).

50. Massaldi, H. A. & Maymó, J. A. Error in handling finite conversion reactor data by the differential method. *J. Catal.* **14**, 61–68 (1969).

51. Wei, J. & Iglesia, E. Isotopic and kinetic assessment of the mechanism of reactions of CH4 with CO2 or H2O to form synthesis gas and carbon on nickel catalysts. *J. Catal.* **224**, 370–383 (2004).

52. Dimian, A. C., Bildea, C. S. & Kiss, A. A. *Integrated Design and Simulation of Chemical Processes*. (Elsevier Science, 2014).

53. Uhlig, H. H. & Revie, R. W. *Corrosion and corrosion control. An introduction to corrosion science and engineering. Third Edition.* (1985).

54. Mosallanejad, S., Dlugogorski, B. Z., Kennedy, E. M. & Stockenhuber, M. On the Chemistry of Iron Oxide Supported on γ-Alumina and Silica Catalysts. *ACS Omega* **3**, 5362–5374 (2018).

55. Suttiponparnit, K. *et al.* Role of Surface Area, Primary Particle Size, and Crystal Phase on Titanium Dioxide Nanoparticle Dispersion Properties. *Nanoscale Res. Lett.* **6**, 1–8 (2011).

56. Maldonado, C. S. *et al.* Low concentration fe-doped alumina catalysts using sol-gel and impregnation methods: The synthesis, characterization and catalytic performance during the combustion of trichloroethylene. *Materials (Basel).* **7**, 2062–2086 (2014).

57. Trueba, M. & Trasatti, S. P. γ-alumina as a support for catalysts: A review of fundamental aspects. *Eur. J. Inorg. Chem.* 3393–3403 (2005) doi:10.1002/ejic.200500348.

58. Greffié, C., Benedetti, M. F., Parron, C. & Amouric, M. Gold and iron oxide associations under supergene conditions: An experimental approach. *Geochim. Cosmochim. Acta* **60**, 1531–1542 (1996).

59. Zanella, R., Giorgio, S., Henry, C. R. & Louis, C. Alternative methods for the preparation of gold nanoparticles supported on TiO2. *J. Phys. Chem. B* **106**, 7634–7642 (2002).

60. Peuckert, M., Coenen, F. P. & Bonzel, H. P. On the surface oxidation of a gold electrode in 1N H2SO4 electrolyte. *Surf. Sci.* **141**, 515–532 (1984).

61. Bonelli, R., Zacchini, S. & Albonetti, S. Gold/iron carbonyl clusters for tailored Au/FeOx supported catalysts. *Catalysts* **2**, 1–23 (2012).

62. Schubert, M. M. *et al.* CO oxidation over supported gold catalysts -"Inert" and 'active' support materials and their role for the oxygen supply during reaction. *J. Catal.* **197**, 113–122 (2001).

63. Hutchings, G. J. Catalysis by Gold: Recent Advances in Oxidation Reactions. *Nanotechnol. Catal.* 39–54 (2007) doi:10.1007/978-0-387-34688-5_4.

64. Vradman, L., Landau, M. V., Kantorovich, D., Koltypin, Y. & Gedanken, A. Evaluation of metal oxide phase assembling mode inside the nanotubular pores of mesostructured silica. *Microporous Mesoporous Mater.* **79**, 307–318 (2005).

65. Boahene, P. E., Soni, K. K., Dalai, A. K. & Adjaye, J. Application of different pore diameter SBA-15 supports for heavy gas oil hydrotreatment using FeW catalyst. *Appl. Catal. A Gen.* **402**, 31–40 (2011).

66. The Buriak Group Data Plotter. Average Shifted Histograms (ASH) in your browser. https://maverick.chem.ualberta.ca/plot/ash.

67. Tang, H. *et al.* Classical strong metal–support interactions between gold nanoparticles and titanium dioxide. *Sci. Adv.* **3**, 1–9 (2017).

68. Liu, X. *et al.* Strong metal-support interactions between gold nanoparticles and ZnO nanorods in CO oxidation. *J. Am. Chem. Soc.* **134**, 10251–10258 (2012).

69. Wang, R., Li, Y., Shi, R. & Yang, M. Effect of metal-support interaction on the catalytic performance of Ni/Al2O3 for selective hydrogenation of isoprene. *J. Mol. Catal. A Chem.* **344**, 122–127 (2011).

70. Bus, E., Miller, J. T. & Van Bokhoven, J. A. Hydrogen chemisorption on Al2O3-supported gold catalysts. *J. Phys. Chem. B* **109**, 14581–14587 (2005).

71. Blosi, M. *et al.* Bimetallic nanoparticles as efficient catalysts: Facile and green microwave synthesis. *Materials (Basel).* **9**, 1–25 (2016).

72. Hosseynizadeh Khezri, S., Yazdani, A. & Khordad, R. Pure iron nanoparticles prepared by electric arc discharge method in ethylene glycol. *EPJ Appl. Phys.* **59**, 1–6 (2012).

73. Khoudiakov, M., Gupta, M. C. & Deevi, S. Au/Fe2O3 nanocatalysts for CO oxidation: A comparative study of deposition-precipitation and coprecipitation techniques. *Appl. Catal. A Gen.* **291**, 151–161 (2005).

74. Saira, F., Firdous, N., Qureshi, R. & Ihsan, A. Preparation and catalytic evaluation of Au/γ-Al2O3nanoparticles for the conversion of 4-nitrophenol to 4-aminophenol by spectrophotometric method. *Turkish J. Chem.* **44**, 448–460 (2020).

75. Fang, C. *et al.* Highly Dispersed Pt Species with Excellent Stability and Catalytic Performance by Reducing a Perovskite-Type Oxide Precursor for CO Oxidation. *Trans. Tianjin Univ.* **24**, 547–554 (2018).

76. Spreitzer, D. & Schenk, J. Reduction of Iron Oxides with Hydrogen—A Review. *Steel Res. Int.* **90**, (2019).

77. Lee, D.-W., Yun, J.-Y., Shin, S.-M., Kim, I.-S. & Wang, J.-P. Study on the Reduction of Forging Oxide Scale using Hydrogen. *J. Korean Powder Metall. Inst.* **20**, 174–179 (2013).

78. Yaakob, Z., Bshish, A., Ebshish, A., Tasirin, S. M. & Alhasan, F. H. Hydrogen production by steam reforming of ethanol over nickel catalysts supported on sol gel made alumina: Influence of calcination temperature on supports. *Materials (Basel).* **6**, 2229–2239 (2013).

79. Perdomo, A., Arteaga, G., Sánchez, J. & Rodríguez, D. Influencia del estaño sobre la actividad catalítica del níquel soportado sobre alúmina para la hidrogenación selectiva del acetileno Influence of tin on the catalytic activity of alumina-supported nickel for acetylene selective hydrogenation. *Rev. Técnica la Fac. Ing. Univ. del Zulia* **40**, 69–76 (2017).

80. Dias Ribeiro de Sousa Martins, L. M. *et al.* Supported Gold Nanoparticles as Reusable Catalysts for Oxidation Reactions of Industrial Significance. *ChemCatChem* **9**, 1211–1221 (2017).

81. Barbosa, A. L., Herguido, J. & Santamaria, J. Methane combustion over unsupported iron oxide catalysts. *Catal. Today* **64**, 43–50 (2001).

82. Hutchings, G. J. & Kiely, C. J. Strategies for the Synthesis of Supported Gold Palladium Nanoparticles with Controlled Morphology and Composition. *Acc. Chem. Res.* **46**, 1759–1772 (2013).

83. Soubaihi, R. M. Al, Saoud, K. M. & Dutta, J. Critical review of low-temperature CO oxidation and hysteresis phenomenon on heterogeneous catalysts. *Catalysts* **8**, (2018).

84. Rombi, E. *et al.* Gold nanoparticles supported on conventional silica as catalysts for the low-temperature CO oxidation. *J. Mol. Catal. A Chem.* **404**–**405**, 83–91 (2015).

85. Carabineiro, S. A. C. Supported Gold Nanoparticles as Catalysts for the Oxidation of Alcohols and Alkanes. *Front. Chem.* **7**, (2019).

86. Costello, C. K., Kung, M. C., Oh, H. S., Wang, Y. & Kung, H. H. Nature of the active site for CO oxidation on highly active Au/γ-Al2O3. *Appl. Catal. A Gen.* **232**, 159–168 (2002).

87. Parravano, G. Surface reactivity of supported gold. II. Hydrogen transfer between benzene and cyclohexane. *J. Catal.* **18**, 320–328 (1970).

88. Ptáček, P. Processes during Thermal Treatment. *Strontium Aluminate - Cem. Fundam. Manuf. Hydration, Setting Behav. Appl.* (2014) doi:10.5772/58609.

89. Naderi, M. Surface Area : Brunauer – Emmett – Teller (BET). in *Progress in filtration and Separation* 585–608 (2015). doi:10.1016/B978-0-12-384746-1.00014-8.

90. Casapu, M. *et al.* Origin of the Normal and Inverse Hysteresis Behavior during CO Oxidation over Pt/Al2O3. *ACS Catal.* **7**, 343–355 (2017).

Appendices

Appendix A. Characterization of $HAuCl_4$ dissolution synthesized.

The prepared solution of $HAuCl_4$ was studied in terms of the representative $[AuCl_4^-]$ complex. The complex was identified by UV-vis spectroscopy. The characteristic wavelength between 280-350 nm was observed [28].

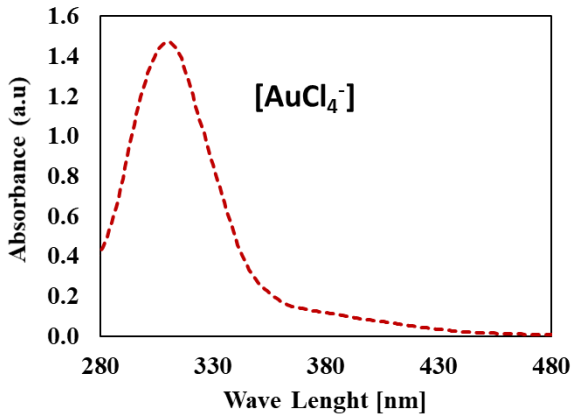

Figure S1. UV-vis spectra of $[AuCl_4^-]$ complex

Appendix B. Characterization of support: surface area and thermal decomposition.

The thermal decomposition of the Al_2O_3 support was studied by thermogravimetric analysis under air. The loss of weight was observed on one step corresponding to the adsorbed water from the atmosphere (Figure S2). A constant weight loss was observed after 300°C. Other small changes in weight were observed at ~500°C and 650°C corresponding to possible decomposition of γ-Al_2O_3 δ-Al_2O_3.[88]

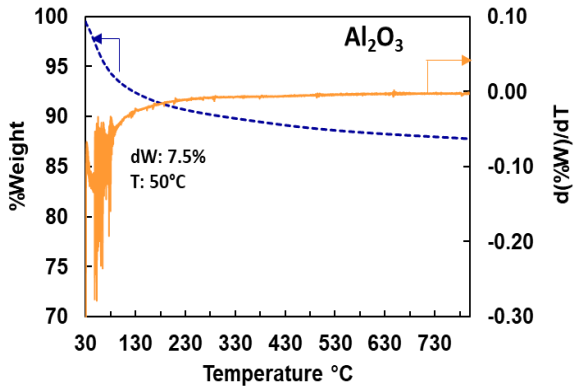

Figure S2. Thermogravimetric analysis of Al_2O_3 under air flow.

The Al_2O_3 was analyzed by N_2 adsorption-desorption. The surface area BET presented a normal hysteresis type IV characteristic of mesoporous material. Also a conventional pore diameter distribution was observed (Figure S3).

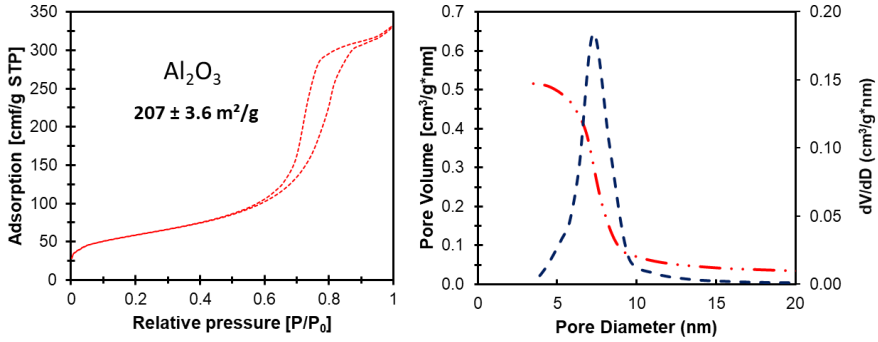

Figure S3. N_2 physisorption, pore volume and diameter distribution of Al_2O_3

Appendix C. Thermogravimetric analysis of a selected catalyst under air and N_2 flow

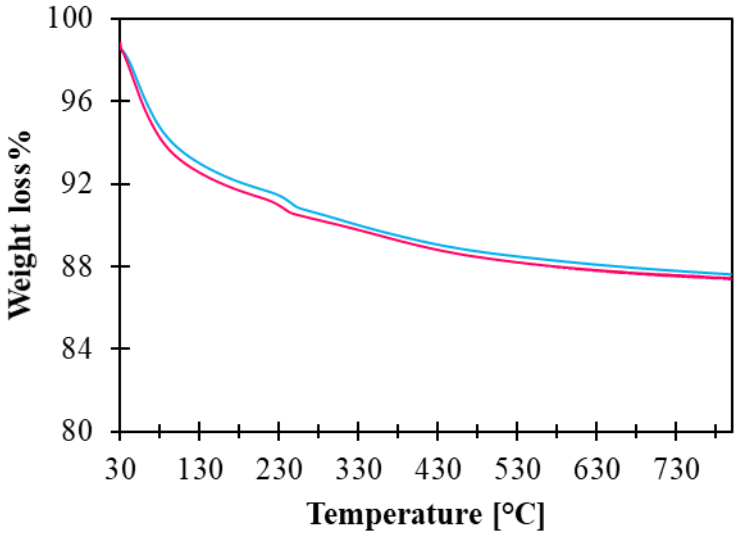

Figure S4. Comparison of thermal decomposition of a selected sample of Au(0.02) under air and N_2 by TGA

Appendix D. N_2 adsorption-desorption isotherm for Au-Fe/Al_2O_3 catalysts

The BET surface area was analyzed before and after catalysts calcination (Figure S5). A decrease the surface areas decreased after calcination was observed. Only the monometallic materials showed a very similar surface area after thermal treatment.

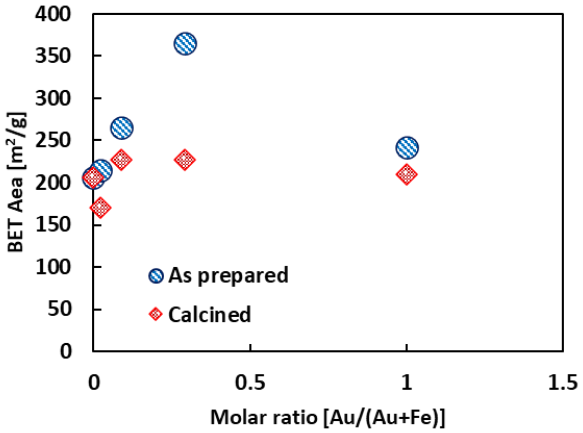

Figure S5. BET Areas comparison from before and after calcination.

N_2 adsorption-desorption isotherms, BJH pore size distribution and cumulative pore volume for catalysts are shown in Figure S6. The figures are shown apart for monometallic Fe(1.00) and integrated in one figure for bimetallic Au-Fe catalysts. In general, all the catalysts showed the same kind of isotherm with plateau at P/P_0 ~ 0.9 and a hysteresis loop closing at P/P_0 ~ 0.65. This is a typical IV type isotherm characteristic of mesoporous materials and inorganic oxides such as alumina[89]. Some differences were observed for Au(0.02) catalyst with lowest surface area and a wide pore size distribution range (2.5 to 15 nm).

The rest of the catalysts presented similar pore size distribution between them, except for the presence of two kind of pores with average sizes of ~4 nm and ~9 nm for the monometallic Au(1.00) catalyst. This aspect was different for the monometallic Fe(1.00) catalyst which

showed only one kind of pore of ~ 10 nm. The differences observed for pore size distributions with respect to gold or iron content in the catalysts are not statistically significant. An analysis with a t-student (95%) determined an confidence interval of 7.2 nm<μ_P<9.1 nm and all catalysts stayed between the tendency. A similar tendency was overserved for surface area and pore volume distribution.

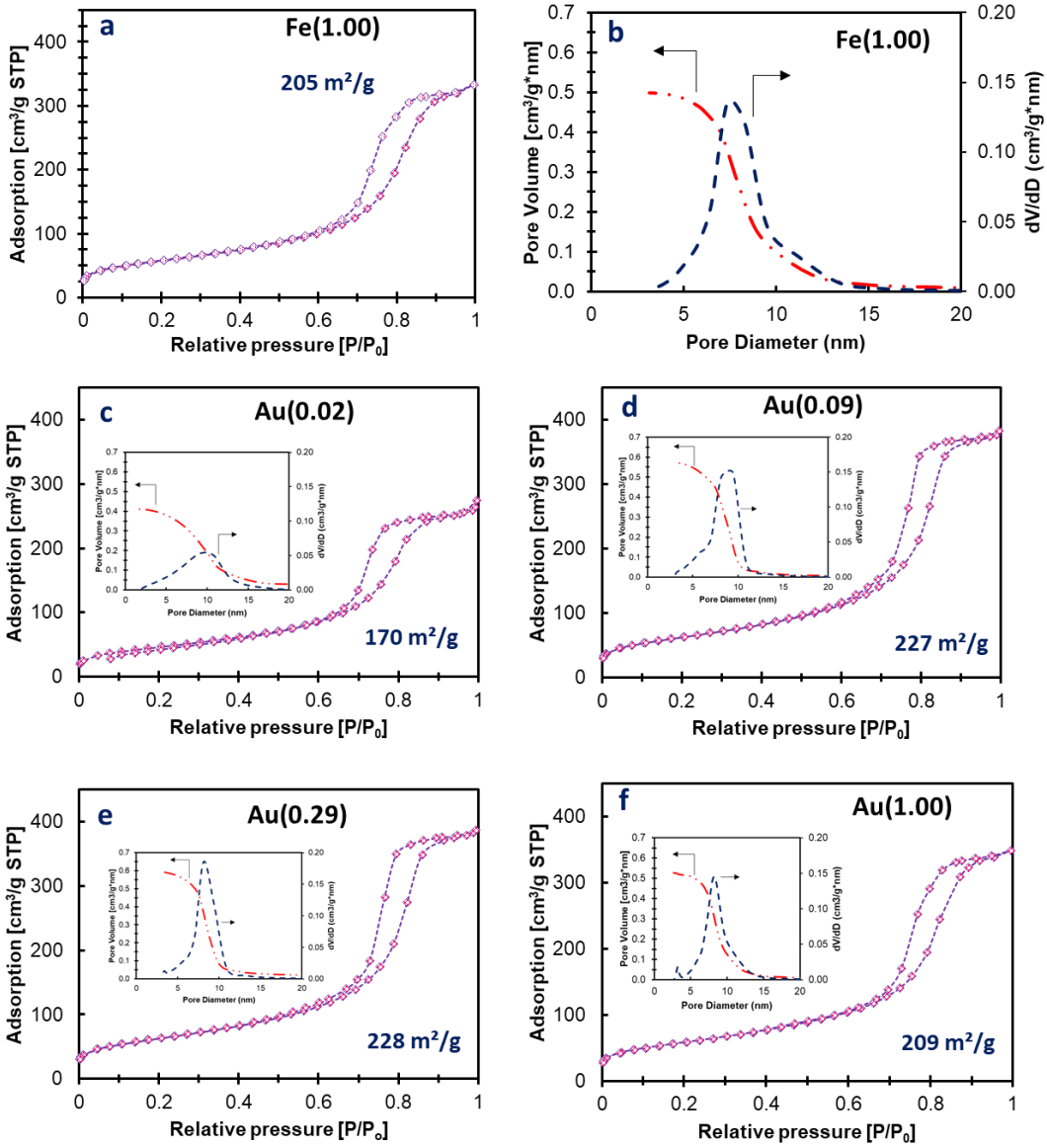

Figure S6. N_2 Adsorption-Desorption Isotherms and BJH pore size distribution and accumulative pore volume of: a) and b) Fe/Al_2O_3, respectively, and integrated figures for c) Au(0.02), d) Au(0.09), e) Au(0.29), f)Au(1.00).

The effect of the gold molar composition of the catalysts over the surface area, volume and pore size distribution was analyzed statistically, as presented in Figure S7. For all the catalysts the tendency was similar, laying into the range of the respective property. The dotted lines represent the maximum and minimum value of the property. Just the lowest gold composition appeared to have a significant effect over all the physical properties, laying outside the confidence interval.

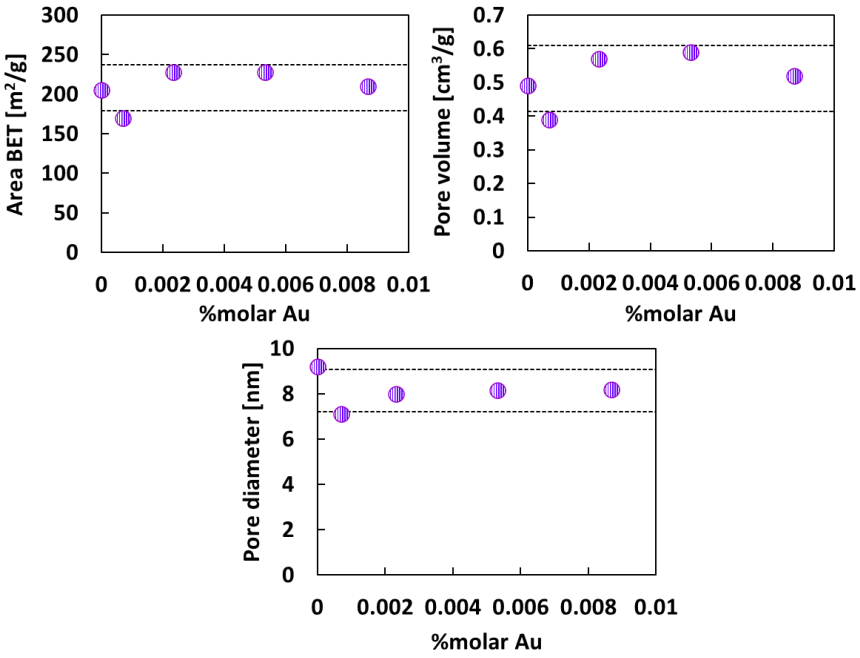

Figure S7. Statistic effect graphics of the metal molar composition over the surface area and porosity properties studied by N_2 physisorption

Appendix E. Summary of N_2 physisorption, PZC and PAD data

The BET surface area, pore volume and diameter observed for Al2O3 decreased after Fe and Au impregnation. On the other hand, the PZC increased after Fe impregnation over Al2O3 but decreased after Au impregnation. The former was related to the addition of hydroxyl groups from de Fe_2O_3 phase which was corroborated with the PAD curve deconvolution, estimating the given values of OH type IIA, IA and IB presented in Table S1.

Table S1. Compilation of surface characteristics for support, monometallic Fe(1.00) and a selected bimetallic Au-Fe catalyst.

Catalyst	**Al_2O_3**	**Fe-Al_2O_3**	***Au(0.02)**
Area BET [m^2/g]	207.73	196.26	170
Pore volume [cm^3/g]	0.50	0.52	0.41
Pore diameter [nm]	9.16	9.2	8.6
[OH]/nm^2	5.16	10.4	2.6
PZC	7.31	7.50	6.22
Type IIA [mmol OH^-/g cat]	1.50	1.67	0.17
Type IA	0.25	0.78	0.56
Type IB	n.d.	1.03	5.69

*Selected catalyst

Appendix F. Effect of metal mol% over dispersion and metal surface area calculated by chemisorption.

The gold and Fe mass percent on the catalysts are marked by circles or squares, respectively. The influence of the metal content over the metal dispersion and metal surface area seems to be null except for the lowest gold content (Figure S8). The latter achieved ca. 60% of dispersion and 1.6 m^2/ g metal.

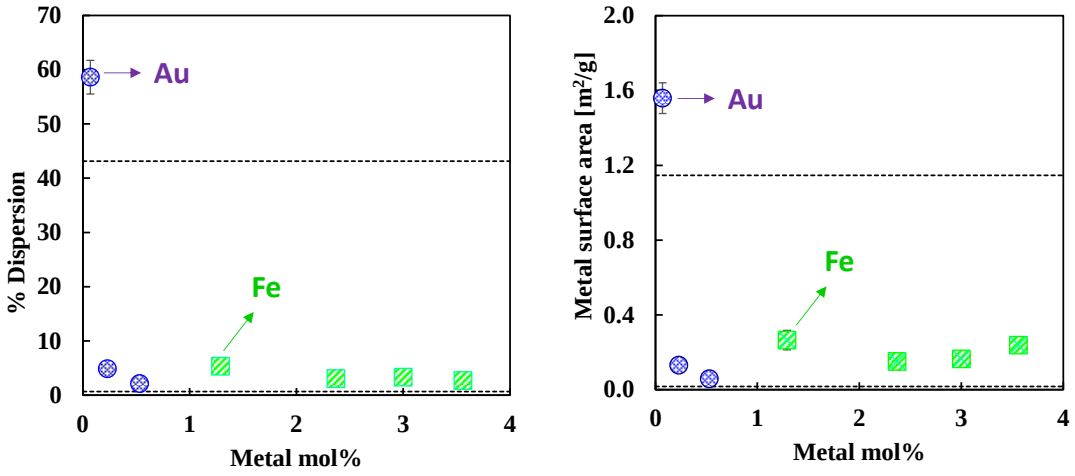

Figure S8. Metal Dispersion and surface area estimated by chemisorption.

Appendix G. Ignition- extinction tests

The ignition -extinction tests between 500 and 750°C are showed below. Inverse hysteresis was observed for all catalysts[90].

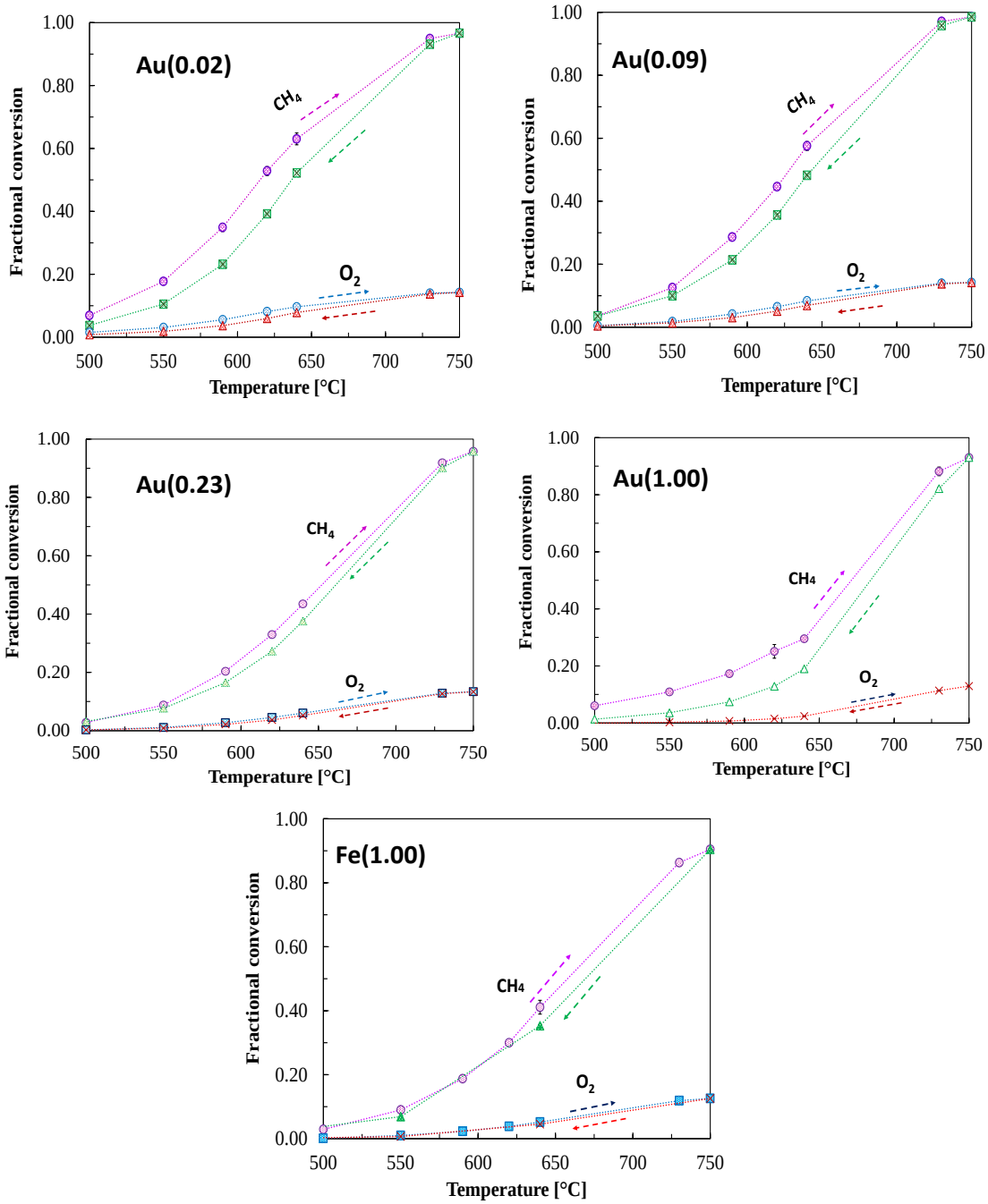

Figure S9. Ignition-extinction reactions for Au-Fe/Al2O3 catalysts including monometallic samples.

Appendix H. Stability tests

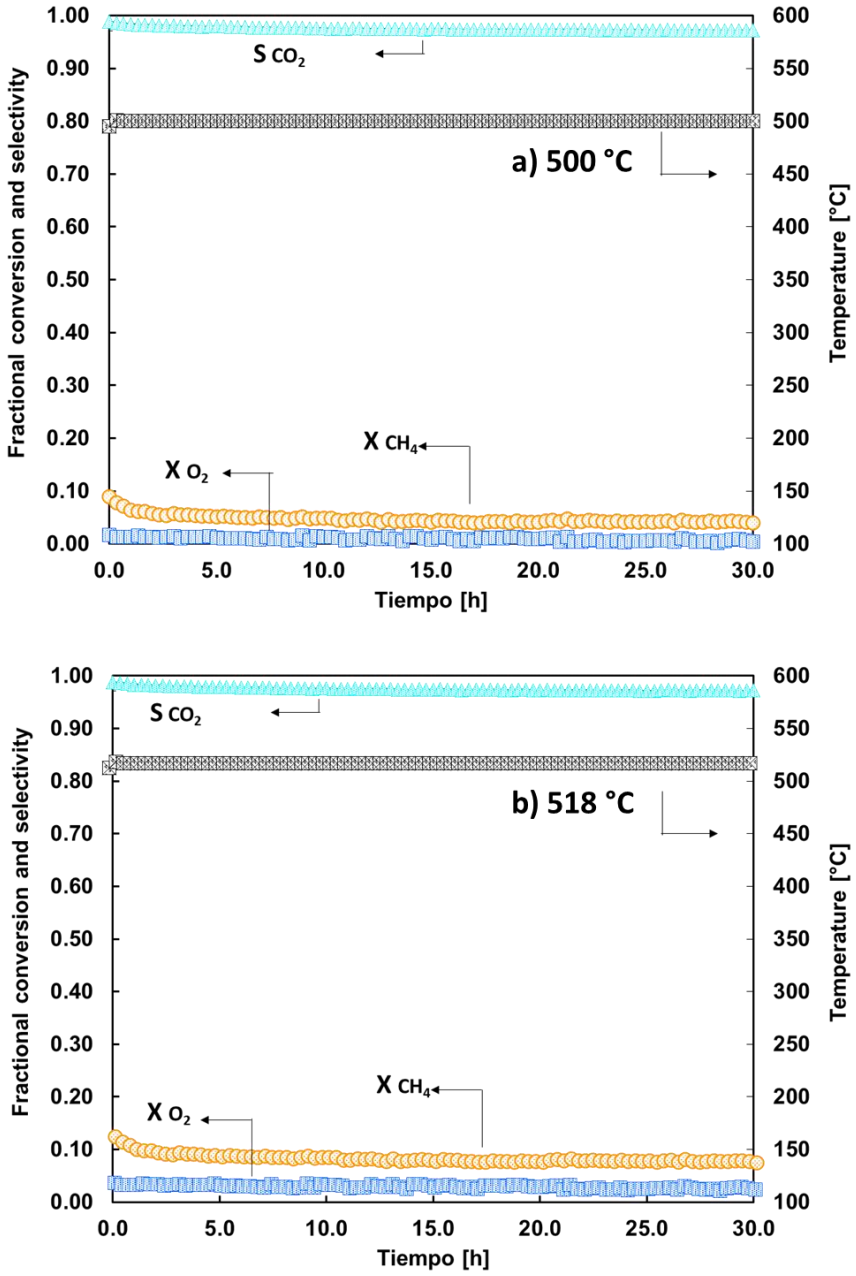

Figure S10. Stability tests for Au(0.02) catalyst at constant temperatures of: a) 500°c and b) 518°C for 30 h. GHSV: 57000 $mL*g^{-1}*h^{-1}$